UNIVERSIDAD DE GUANAJUATO

MASTER THESIS

Design, fabrication and implementation of microfluidics systems applied in chemical micromixers and particle sorters test

Author:
Jonathan Ulises Álvarez Martínez

Supervisor:
Dr. Rigoberto Castro Beltrán

A thesis submitted in fulfillment of the requirements for the degree of Master in Applied Science

in the

Biophotoacoustic Group at the University of Guanajuato

July 29, 2020

Declaration of Authorship

I, Jonathan Ulises Álvarez Martínez, declare that this thesis titled, "Design, fabrication and implementation of microfluidics systems applied in chemical micromixers and particle sorters test" and the work presented in it are my own. I confirm that:

- This work was done wholly or mainly while in candidature for a masters degree at this University.
- Where any part of this thesis has previously been submitted for a degree or any other qualification at this University, this has been clearly stated.
- Where I have consulted the published work of others, this is always clearly attributed.
- Where I have quoted from the work of others, the source is always given. With the exception of such quotations, this thesis is entirely my own work.
- I have acknowledged all main sources of help.
- Where the thesis is based on work done by myself jointly with others, I have made clear exactly what was done by others and what I have contributed myself.

Signed:

Date:

"Thanks to my solid academic and experimental training, today I can write hundreds of words about my topic, this on simulation, theoretical and experimental representation."

UNIVERSIDAD DE GUANAJUATO

Abstract

Master in Applied Science

Design, fabrication and implementation of microfluidics systems applied in chemical micromixers and particle sorters test

by Jonathan Ulises Álvarez Martínez

In this thesis work, the most recent and relevant work related with microfluidics in terms of device fabrication through different techniques with a particular interest on the direct laser writing technique is presented. Direct laser writing technique was the used protocol for the fabrication of the microfluidic master masks under test and the details about the focused light-matter interaction is discussed and demonstrated.
The design and the development of an efficient fabrication protocol of the polymeric microstructures is presented, discussed and justified. COMSOL Multiphysics simulations were carried out for comparison purposes.
The thesis work was focused on two main chips: such as micromixer of chemical species and such as particle sorter. The first one was the main objective of this thesis work and through which all the experimental procedures and the corresponding simulations are presented. The designated geometrical shape was based on a Y-serpentine with channels of 500 μm of width which allowed us to mix two fluids. Fluorescence spectroscopy was used such as the measurement technique to follow the molar concentration evolution and in this way, a commercial dye was used for this purpose with 0.5 $x10^{-6} Mol/L$ of molar concentration resolution. COMSOL Multiphysics simulations of the mixing process reproduced well the experimental results which validates these experiments. The particle sorter device, this is presented such as perspective of this work because some problems in the performance are presented due to limitations on the optical resolution. Nevertheless, details of device design, fabrication and finally, the particle tracking application are presented. This microfluidic chip is composed by two main sections: the inlets and the sorter section. The first part is composed of bigger channels than the sorter region, which contains 4 thin channels followed by another bigger channel that works as outlet. For this microfluidic chip, PMMA particles with 10 μm of diameter were injected inside the chip and their tracking position along the two sections was performed by video microscopy technique. COMSOL simulations of the fluid behavior were, in addition, carried out and compared with those experimentally obtained where, it is noticeable that the velocity of the fluids match well according the experimental observations.
Finally, this thesis work presents the full development of a 3D mechanical platform which reach 1.25 μm of mechanical resolution. The software design that controls it is in addition presented.

Acknowledgements

I would like to give the greatest thanks to my parents, they gave me the inspiration to be a person of good. Specially my mother since she is my role model for personal growth.
Thanks also to my brothers, Claudia who taught me that self-love should be a priority in life, Leonardo for being my life and learning companion and finally, Eduardo for sharing with you the greatest passions of music and be the person who showed me life as real and sweet as it can be, thanks guys without you I probably wouldn't be who I am now.
Dr Rigoberto, thank you for trusting on me and on my potential, specially for giving me challenges that seemed impossible to meet, it was very important in my growth. Dr Gerardo, thank you for always supporting the projects of your students and giving them the vote of confidence that we all need at the beginning, as well as always giving me a place in your group. Dr Ngoc Diep Lai thank you for receiving me as a guest in your research group at the École normale supérieure in Paris, and giving me the opportunity to learn from you.
To my friends Víctor, David Álvarez, Manuel, Ramón, Héctor, Mario, Mauricio and all those who I do not mention, but who know that they are important to me.
I specially want to thank the support of CONACYT throughout the postgraduate period, which also supported me with a MIXED scholarship to carry out research outside the country. In addition, thanks to the project "Retos teóricos-experimentales del ultrasonido inducido por láser en aplicaciones biomédicas: detección de célula de cáncer en circulación, ultrasonido enfocado, e imágenes cuantitativas de tejido canceroso" with number of project: 2029 from *FronTeras de la ciencia*. Thanks also to DAIP, which also gave me financial support to carry out studies and research outside the country, specially to the projects CIIC-2019 and CIIC-2020. Finally thanks to the University of Guanajuato for being my "alma matter". ...

Contents

List of Figures

List of Tables

Dedicatoria ... Para mi bella madre... Tú siempre confiaste en mi y siempre me impulsaste a querer ser el mejor. Te amo mamá. <3

Chapter 1

Introduction

1.1 State of the art

During the past years, the full control and automation of opto-electronic and mechanics devices have been widely employed around a great variety of important scientist research experiment (Noonan et al., 2011; Camarena-Chávez et al., 2020). Specifically, the fabrication of micro- and sub-micrometer optical structures in view of photonics and biochemical applications. Many printing techniques are nowadays presenting such as standard platforms to develop these structures i.e., e-beam lithography (Lin et al., 2017), stereolithography (Bhattacharjee et al., 2016), deep UV-photolithography (Gong et al., 2017), direct laser writing (DLW) (Tong et al., 2017) and so on. The fabrication protocols of these platforms have allowed the micrometer and sub-micrometer developing of simple and complex photonic structures. Standard lithography procedure works more on the transmission pattern from master masks which permits the 2D printing of devices while the fabrication of 3D photonic devices is more limited to extra fabrication steps (Lee et al., 2006). On the other hand, DLW which is carried out from focusing the laser beam on a photo-sensible polymer positioned on a full 3D axes movement mechatronics platform, allows a more suitable 3D printing structure (Camarena-Chávez et al., 2020). The grand acceptance for the scientific community has been mainly because of its high movement and the facility for the pattern printing at the micro- and sub-micrometer scales. Optical gratings (Wang and Tsai, 2004), the photonic crystals printing, electro-valves, radio frequency micro-electro machine (Holmes, 2001), micro-grids for photonic applications (Kishimoto et al., 2009) and the printing of micro-molds (Isiksacan et al., 2016; Joanni et al., 2015) in view of the developing of master masks fabrication for micro-fluidic applications are few of the huge range of potential application through the implementation of these 3D printing systems based on DLW procedures. Many mechatronic platforms are commercially and most of them offer the opportunity to easily develop those mentioned structures without the extraordinary need for high-cost investment. In one hand the cons on it can be referred to the low degree of freedom corresponding to the software design, limiting the creativity of the final users and, in some cases the low robustness of the platforms restricting its transport to other labs and reducing its versatility in terms of potential applications, in the other hand the pros can be summarized in the very high resolution of these platforms. Our group understands the importance of the applied learning and looking for DLW applications based on photosensitive materials, here the full design, implementation and application of a 3D mechatronic platform for microfluidics master masks implementation is presented.

1.2 LOPA based Direct Laser Writing

The optical lithography consists in producing physical changes in a photosensitive polymer resist (SU-8) by coherent radiation (Liaros and Fourkas, 2019). Photoresist are categorized as negative and positive, in one hand the negative photoresist in the irradiated zones turns from viscous to solid and in the other hand the positive resist turns from viscous to solid those no-irradiated zones; for the scope of this thesis work, the used SU-8 is negative (MICROCHEM, 2017). Protocols to transfer specific patterns to the SU-8 have been improved along the last years reaching micro and sub-micrometers structures (Kim et al., 2016; Mao et al., 2017). Nowadays it is well-accepted that there are at least three main mechanisms of light absorption in materials, as shown in Figure 1.1: one photon absorption (OPA) (Sánchez and Carrer, 2016), low-one photon absorption (LOPA) (Nguyen et al., 2016) and two photon absorption (TPA) (Yee et al., 2017). Each phenomenon belongs to a different region of wavelengths, OPA occurs in the strongest absorption region (where the maximum peak is presented),TPA takes place at near the double of the maximum wavelength absorption, in this case high intensity lasers are necessary to produce this nonlinear (NL) absorption, while, the LOPA region can be taken as the region where the material still having the linear absorption (OPA) but, with a very poor efficiently. The selection of each phenomenon and the intensity of light depend entirely on the desires scale and application.

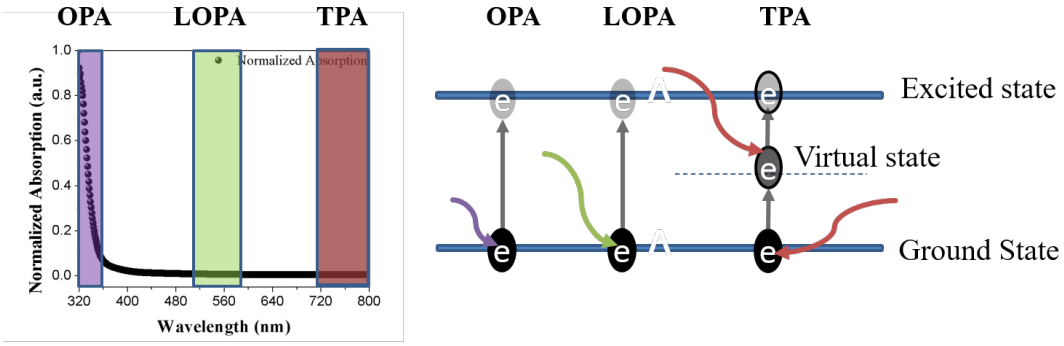

FIGURE 1.1: a)Absorption spectrum of the employed photoresist, where observed different absorption regions and b) the molecule energy level representation.

OPA is a linear absorption phenomenon in which one photon is necessary to excite the molecule from the ground state to an excited state; in the case of TPA the NL combination of two photons to carry out the process from the ground to the excited state which is possible by employing high peak intensities of laser excitation (LaFratta and Baldacchini, 2017; Fourkas, 2020). Both phenomena have been widely employed in the fabrication of micro electro-machines (MEMs) and microstructures, for example, there exist fabrication of by using a fs laser at 833nm which allows structures at the microscale but the equipment is highly costly. In the other hand, in the LOPA region, where the absorption of photons is very low compared with OPA, it is possible to increase the penetration depth in the sample and the implementation cost is reduced. Taking advantage of this, by LOPA it is possible to polymerize thick films (>25 μm) of SU-8 photoresist. When both the DLW protocol and the LOPA phenomenon are considered as parts of the full fabrication procedure of a 3D automated

mechatronic platform, the printing of micrometer structures are achievable by using a continuous wave (CW) laser.

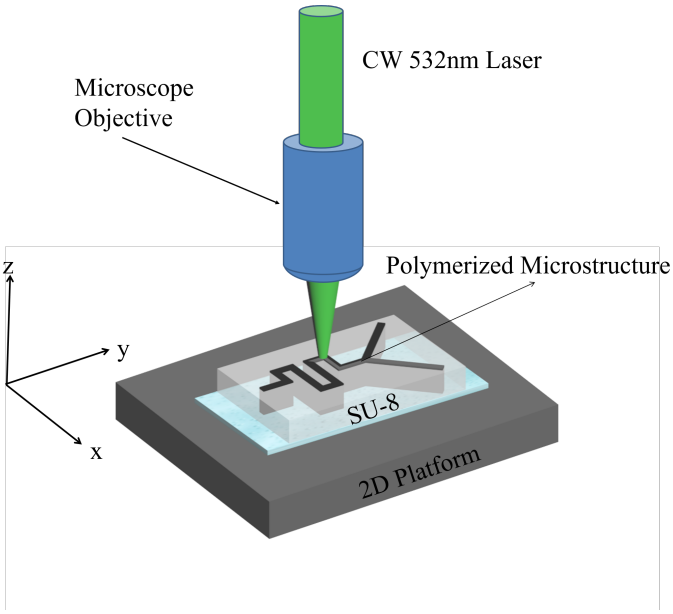

FIGURE 1.2: Artistic illustration of LOPA based DLW.

As it is showed in Figure 1.2, to polymerize the SU-8 photoresist, it is necessary to irradiate specific zones of the SU-8 film, forming covalent bonds to join two polymer chains together which is also know it as crosslinked (black) while those that were not irradiated (translucent) remain soluble and can be "washed" in a revealed bath leading only solid polymerized SU-8.

This SU-8 solid, placed on the soda lime glass (SLG) substrate is considered as a Master Mask and can be employed to produce molds of microchannels. Without considering neither the scatter of light and the thermo-optical effect during the polymerization process, the laser writing resolution (optically) is governed by the Rayleigh limit. This "optical limit" will be related with both the numerical aperture of the used optical microscope objective and the working wavelength.

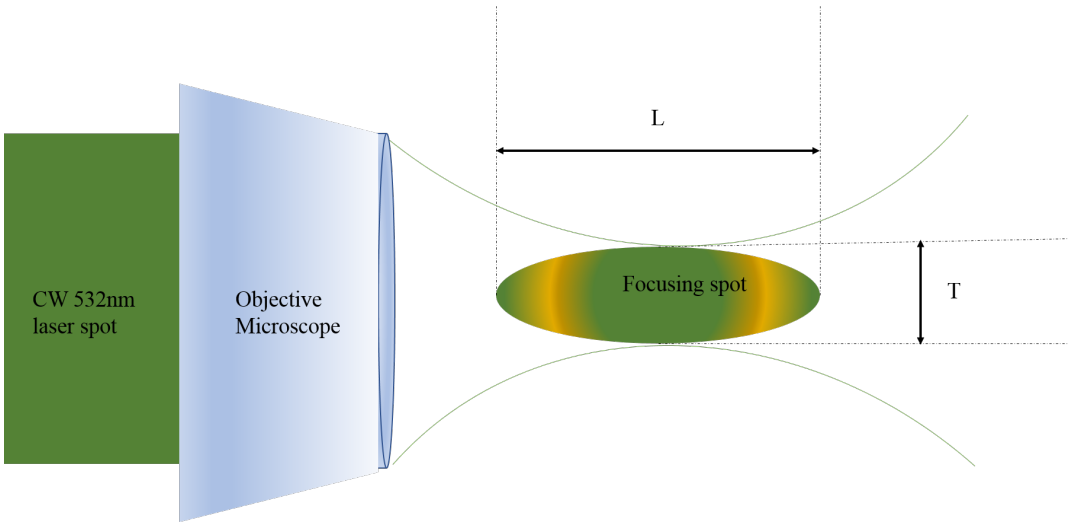

FIGURE 1.3: Representation of the involved parameters when a laser beam is highly focused by a microscope objective.

From Figure 1.3, it is possible to observe the spatial distribution when a laser beam is focused by a specific microscope objective. It is observed that both the longitudinal L and the transversal T parameters define entirely the focused light when a microscope objective is used (Do, 2015; Li, 2014).

$$\frac{T}{2} = \frac{0.61\lambda}{NA} \tag{1.1}$$

and

$$\frac{L}{2} = \frac{2\lambda}{NA^2} \tag{1.2}$$

According with these equations, we keep fixed the wavelength "λ", thus, to printing shorter optical pattern it is necessary to variate the numerical aperture (NA).

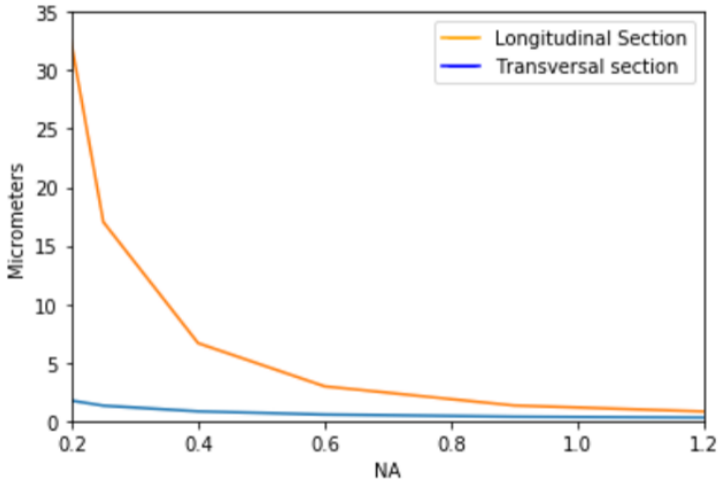

FIGURE 1.4: Comparison between the longitudinal and transversal section of the focused spot.

From Figure 1.4 it can be observed that T and L converge when the NA increase, this permits that T and L becomes similar. When the parameters T and L are modeled as the semi-axes in the ellipse, the variation of NA results in the variation of the focused spot. To better represent how the light distributes along the air-material interface once this passes through a microscope objective, the Wolf-Debye Theory can be used to model the confinement of a laser beam and its spatial distribution changes, varying the NA, this will be described in the next section.

1.3 Wolf Debye Theory

As it is mentioned above, the focusing region of the laser beam can be modified by varying the numerical aperture of a microscope objective (MO). This selection affects the physical parameters of the focusing region (Rayleigh Waist) which results in a modification of the intensity profile. Through the Wolf-Debye theory (Wolf and Li, 1981) it is possible to plot the spatial distribution of the very focused electromagnetic field along a particular material. The next equation 1.3 describes the spatial distribution of the laser beam according to the incident beam mode ($\mathbf{A}(\theta, \phi)$), the apodization factor ($\mathbf{B}(\theta, \phi)$) and the polarization ($\mathbf{P}((\theta, \phi)$) (Foreman et al., 2008). Details of the matrix polarization can be consulted in Article reference: (Camarena-Chávez et al.,

2020).

$$\mathbf{E}(x,y,z) = -\frac{iC}{\lambda}\int_0^{\alpha}\int_0^{2\pi} \sin\theta \mathbf{A}(\theta,\phi)\mathbf{B}(\theta,\phi)\mathbf{P}(\theta,\phi)e^{ikn(z\cos\theta + x\sin\theta\cos\phi + y\sin\theta\sin\phi)}d\theta d\phi \tag{1.3}$$

The letters in bold represent vectors and where λ is the laser wavelength and C the speed of light in the vacuum. Through equation 1.3, the spatial distribution is plotted and presented in Figure 1.6. To visualize the angles references for θ and ϕ Figure 1.5 shown the angular parameters under a Gaussian reference sphere.

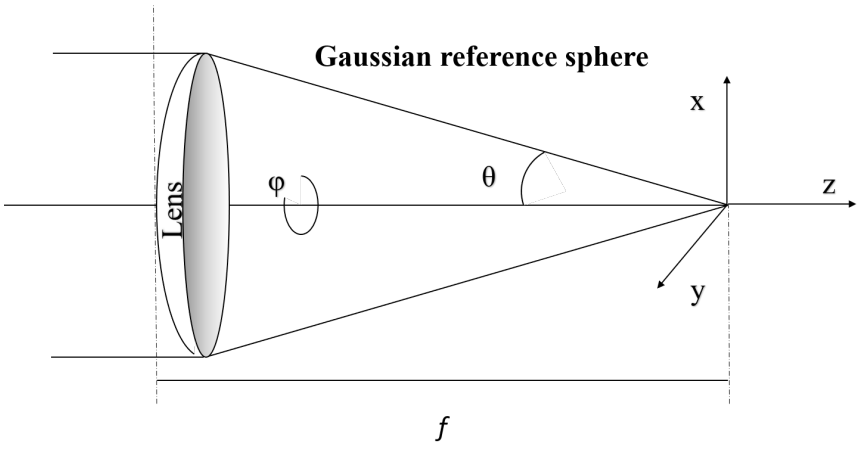

FIGURE 1.5: Gaussian reference sphere for θ and ϕ angles.

The angular dependency for NA = $\eta sin\theta$ where η is the refractive index of the media. The numerical simulations were done by considering three different NA: 0.13, 0.25 and 0.40 and by considering air as medium.

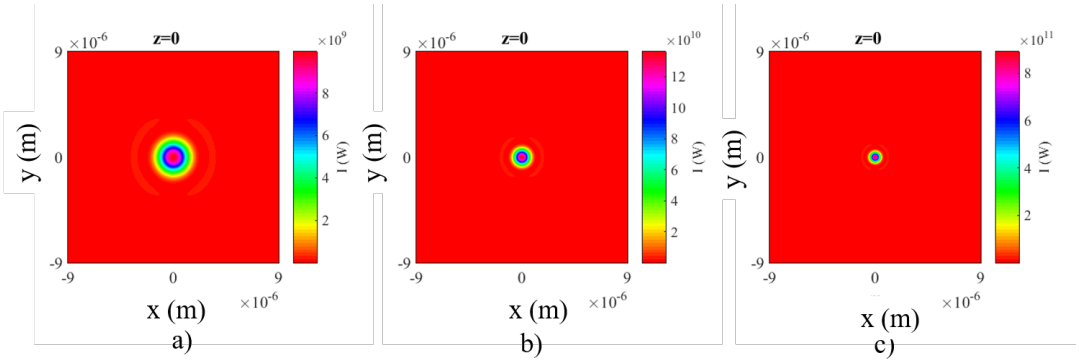

FIGURE 1.6: The spatial distribution of the focused electromagnetic field using a) 0.13, b) 0.25 and c) 0.40 numerical apertures, corresponding to objective microscopes of 5x, 10x and 20x, respectively.

From Figure 1.6, the electromagnetic field distributes in a shorter area as the NA increase; these numerical simulations were carried out at z=0 (the focal distance). In addition, Figure 1.6 shows that by using higher NA it is possible to fabricate smaller polymeric structures, if we fulfill the required experimental parameters. Moreover, the intensity is enhanced with higher NA, thus, the exposure and the fabrication time can be reduced given the increasing energy per unit of area.

When two different interfaces are now considered, i.e., air/SU-8, the equation 1.3 changes as follows:

$$\mathbf{E}(x,y,z) = -\frac{iC}{\lambda}\int_0^{\alpha}\int_0^{2\pi} \sin\theta_1 \mathbf{A}(\theta_1,\phi)\mathbf{B}(\theta_1,\phi)\mathbf{P}(\theta_1,\theta_2,\phi)$$
$$e^{ikn(\eta_2 z cos\theta_2 + \eta_1 x sin\theta_1 cos\phi + \eta_1 y sin\theta_1 sin\phi)} + \Phi(\theta_1,\theta_2,\phi)\mathrm{d}\theta_1\mathrm{d}\phi \tag{1.4}$$

From equation 1.4 the different refractive indexes η_1 and η_2 of the involved media, the sample thickness z, the induced aberration Φ and the focused electromagnetic field are considered. The respective numerical simulations from Equation 1.4 are presented in Fig1.7 by considering the different microscope objectives used above. In addition, numerical simulations were done at different z values with the goal of demonstrated the feasibility of these equation to present how the electromagnetic field is distributed along the interface under different experimental conditions. From numerical simulations, it is noticeable that through Wolf-Debye theory is not possible to model does the spatial field distribution for z values above 20 μm (for the particular case of NA=0.40). Specifically, it is observable a no-homogeneous spatial distribution of the field which is a critical point for this theory that appear be senseless for those value of z close to the focal length z=0. However, this give us the opportunity to correctly visualize how the field distribution occupies a bigger area as the NA is higher and the microscope objective (MO) is positioned far from z= 0 μm. (Camarena-Chávez et al., 2020; Wolf and Li, 1981)

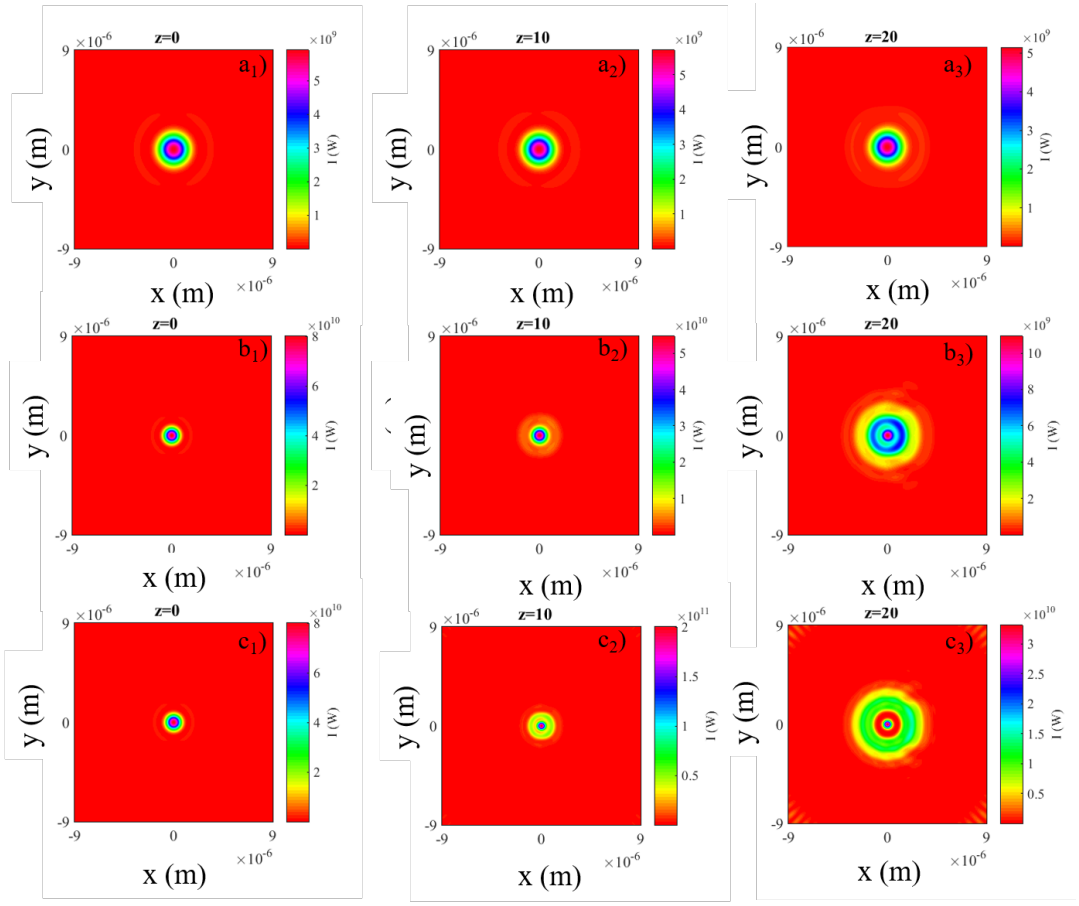

FIGURE 1.7: Numerical simulations of the focused electromagnetic spatial distribution passing through the interface Air/SU-8, plotted at different z-planes 0, 10 and 20 μm, these numerical simulations were carried out by following the equation 1.4

In Figure 1.4 it can be observed the spatial distribution of the focused electromagnetic field for different NA and z-planes, from top to bottom the variation in the NA and from left to right the variation in the z-plane. As can be noticed, when the MO is unfocused and by considering the higher NA, the divergence of the spatial distribution occurs for small distances away from z=0, compared with a lower NA. This is not a limitation to achieve bigger diameters of fabrication. This can be visualized easily if the XY spatial distribution is plotted, in this, the modification of the T and L parameters can be observed. In summary, with higher NA and under unfocused conditions, our experiments will be far away to reproduce the expected optical resolution to the master mask fabrication, the support information for this is showed in Camarena-Chávez et al., 2020 through COMSOL simulation. Briefly, table 1.1 shows the expected optical limit for the three different microscope objectives presented above, from equations 1.1 and 1.2.

NA	T(μm)	L(μm)
0.13	4.9	16.3
0.25	2.5	8.5
0.40	1.6	5.3

TABLE 1.1: Theoretical values for the longitudinal and transversal section of the focused electromagnetic field

Finally, the derived application from those printing structures are more focused on photonic platforms where these devices controls light for many technological purposes. For the scope of this thesis work, the unfocused condition was not at all critical, nevertheless, the field amplitude played an important role at the end of the fabrication process.

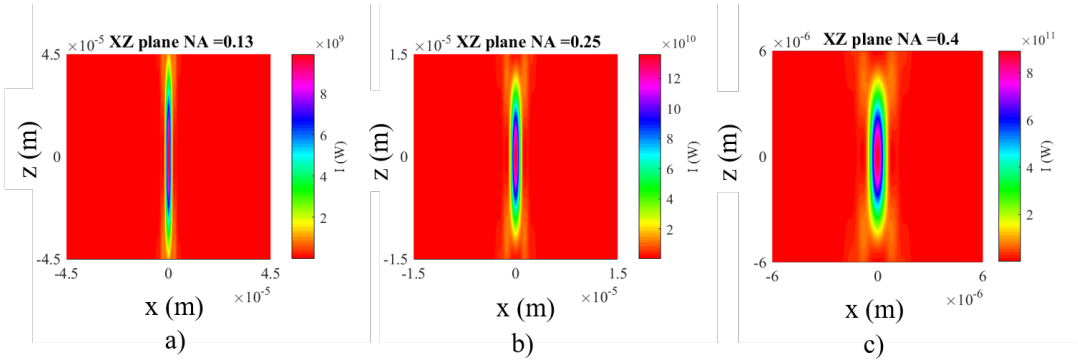

FIGURE 1.8: Spatial distribution of the focused laser beam in the XZ plane, these numerical simulations were carried out for NA values of a) 0.13, b) 0.25 and c) 0.40

From Figure 1.8, it is deduced that for low NA, at the Z-direction, the field distribution is larger compared with the higher NA with penetration depth that respectively range from 90 μm to 12μm. Figure 1.8, in addition, allows us to visualize how the symmetry condition, along the Z-axis (transverse cut) at the end (top and bottom) of each numerical simulation, gets lost as the NA is higher which demonstrated that the Wolf Debye theory does not resolve at all how field distributes at particular z values (Camarena-Chávez et al., 2020). The microfluidic devices were finally fabricated by using the MO with NA=0.25.

1.4 Microfluidic Systems

The manipulation of fluids at the macroscale have been studied for centuries, but nowadays the control and manipulation of fluids at the microscale has an important roll in different branches of the science, as it was mentioned in section 1.1, microfluidic systems are systems designed and fabricated with micron sizes with the aims to manipulate fluid for different purposes. An important effect is the surface to volume ratio which is very high, so any chemical reaction in a microfluidic is greatly accelerated. Those systems that are fabricated to diagnostic and/or treatment of illness are called lab-on-a-chip (LOC).

The equation that govern the fluid motion in both the macro- and micro-scale is built on the fundamental laws of conservation and is know it as the Navier-Stokes equation, it is possible to deduce this equation by considering the Newton's Law $F = m\frac{\partial \vec{u}}{\partial t}$ for the velocity of a Newtonian fluids as the representation of force-densities for a continuum media:

$$\rho D_t \vec{u} = \rho(\frac{\partial \vec{u}}{\partial t} + (\vec{u} \cdot \vec{\nabla})\vec{u}) = \sum_j f_j \tag{1.5}$$

The operator $D_t = \frac{\partial}{\partial t} + \vec{u} \cdot \nabla$ represents the total time derivatives applied on the fluid velocity ($\vec{u}$).
In general, in fluids, the two force densities acting in micro-scale systems are the

force due the viscosity "$\mu\nabla^2\vec{u}$" and the pressure changes "$-\nabla p$". Considering this and equation 1.5, the resulting equation is the Naiver-Stokes equation (Papautsky, Ameel, and Frazier, 2001):

$$-\vec{\nabla}p + \mu\nabla^2\vec{u} = \rho[\frac{\partial\vec{u}}{\partial t} + (\vec{u}\cdot\vec{\nabla})\vec{u}] \tag{1.6}$$

Where μ, ρ and p are respectively the dynamic viscosity, density and pressure of the fluid within a microchannel. To the right of the equation, the inertial accelerations appear and to the left the involved viscosity forces. In this equation 1.6, the gravitational and electrical forces $\vec{f} = \vec{f_{grav}} + \vec{f_{el}} = \rho\vec{g} + \vec{\rho_{el}}\vec{E}$ have been neglected given the very small amount of fluid.
By considering the mass conservation equation such as:

$$\frac{\partial\rho}{\partial t} + \nabla\cdot(\rho\vec{u}) = 0 \tag{1.7}$$

if ρ is constant along the microchannel. Equation 1.7 becomes

$$\nabla\cdot\vec{u} = 0 \tag{1.8}$$

Which permits to notice that the fluid cannot vanish into nowhere or arise from nowhere. Taking this into consideration, for p and ρ constants, any change in the velocity of the fluid it is due to changes in the hydraulic diameter D_h. Assuming that, the velocity of the fluid $\vec{u}$ changes inversely with D_h, thus, any change in the velocity $\vec{u}$ will be proportional to $\frac{1}{D_h}$ (Prakash, Pinti, and Bhushan, 2012).

From this, it is possible to compare the effect between the inertial and viscous forces into a microchannel and presented throughthe next equation:

$$\frac{\mid\rho(\vec{u}\cdot\vec{\nabla})\vec{u}\mid}{\mid\mu\nabla^2\vec{u}\mid} = \frac{\rho u_0^2/D_h}{\mu u_0/D_h^2} = \frac{\rho u_0 D_h}{\mu} \tag{1.9}$$

The ratio between forces results in a dimensionless quantity number that is commonly called the Reynolds number (Re). This Re number is widely used to classify the flow regime of the fluids in both, micro- and macro-scale. For instance, fluids can be classified in terms of the Re (Zhang et al., 2016).

1.5 Mixing Process in Microfluidics

Microscale devices are nowadays consider such as an emergent technologies designated to solve problems that cannot be solved at the macro-scale (Baroud et al., 2003). For example, many biochemical test aims for better biosensors with higher performance in terms of lower required sample (μL), with opportunity to re-used the device, with multi-tasks and finally with the sufficient integrated technology to simply access to a medical diagnostic (in real time) through e-technology. These technologies have been addressed directly in applications related with biological, medical and chemical branches. Nowadays, those systems are know as Lab-On-a-Chip (LOC) technologies (Wu et al., 2016; Suryawanshi et al., 2018). LOC are applied for the control and manipulation of fluids, with the aim to droplet generation, microparticles selection-separation and mixing process are named microfluidics devices.
The fluids which interact within the microfluidic devices are under the same laws

that govern and describes the fluids interactions at the macroscale, but, because miniaturization some additional characteristics are granted to the fluids and these can enhance the execution of many different processes not presented at the macroscale. The main physical aspect behind that enhances the characteristics at the micro-scale are the surface area to volume ratio, diffusion phenomenon and surface tension, between others. In addition, smaller reagents volumes, parallel operations, shorter reaction and mixing time represent a very high control and manipulation of a great variety of fluids i.e. diffusion species (Lee et al., 2016; Lee et al., 2011).

At the micro-scale, the interaction between fluids are usually described as a continuum model, and discrete quantities like force where the mass becomes continuous fields. At the micro-scale, specifically microfluidics systems, this consideration remains valid due to even very small volumes contain a high amount of molecules, Avogadro number, large enough to keep valid the hypothesis (Lagus and Edd, 2013; Zimmerman, 2006). There exist two principal types of microfluidics systems: passive and active systems which for general process these can be classified such as active and passive methods (Lagus and Edd, 2013). Active methods include the use of external forces e.g., electric fields, electrophoresis and pressure variation while the passive method takes advantages of the microchannel geometries.
Taking in consideration the passive methods we can find a interesting application in the biological and medical branches: micromixers. The Figure 1.9 shows the most recent work in passive microfluidic devices, specifically those applied as micromixers. This explanation will be well defined below. Devices based on turbulent fluid have been applied for many purposes, for example (Strachan et al., 2019) applied this to produce cell cultivation meanwhile (Kumaran and Bandaru, 2016) applied a similar device to produce chemical reactions.

Another way to produce turbulent flow is through geometries based on obstacles. Obstacles in the micrometer channels ensure no more well-defined flow-streamlines long these. For example in (Wangikar, Patowari, and Misra, 2018), the device no necessarily achieve the Re >100 oppositely here the reported Re<1, however, the device geometry is based on obstacles which ensure the turbulent conditions to achieve the mixing phenomenon. In addition, (Bahei Islami and Ahmadi, 2019) take advantage of this obstacles within the mixing channel to simulate the mixing degrees along the microchannel. Those systems can efficiently produce mixing effect in a short time and length but the monitoring of the mixture can be impossible precisely because the mixing-phenomenon is variable along the full-device. On the other hand, devices based on the diffusion phenomenon is ideal to both efficiency achieve a mixing effect and to allow the monitoring of this process at whatever point along the device. For example, (Somaweera, Ibraguimov, and Pappas, 2016) applied a Y-micromixer device based on diffusion phenomenon to produce a gradient concentration of drug and test its toxicity over a cell cultivation positioned along the mixing channel while (Keshmiri et al., 2019) applied this Y-micromixer device (serpentine shape) to measure the mass transfer of fluid.

The devices used by (LaFratta et al., 2015) and (Lim et al., 2018) have been fabricated throughthe direct laser writing technique and soft-lithography process while in (Au et al., 2016), the microfluidic devices presented a 3D shape showing the high versatility of the DLW technique to fabricate these kind of devices. Figure 1.9 shows the micromixers discussed above and others which have been developed in the last years. In this thesis work our microfluidics devices will based on both passive methods and these will be fabricated by using the combined DLW and Soft-lithography procedures(Hessel, Löwe, and Schönfeld, 2005).

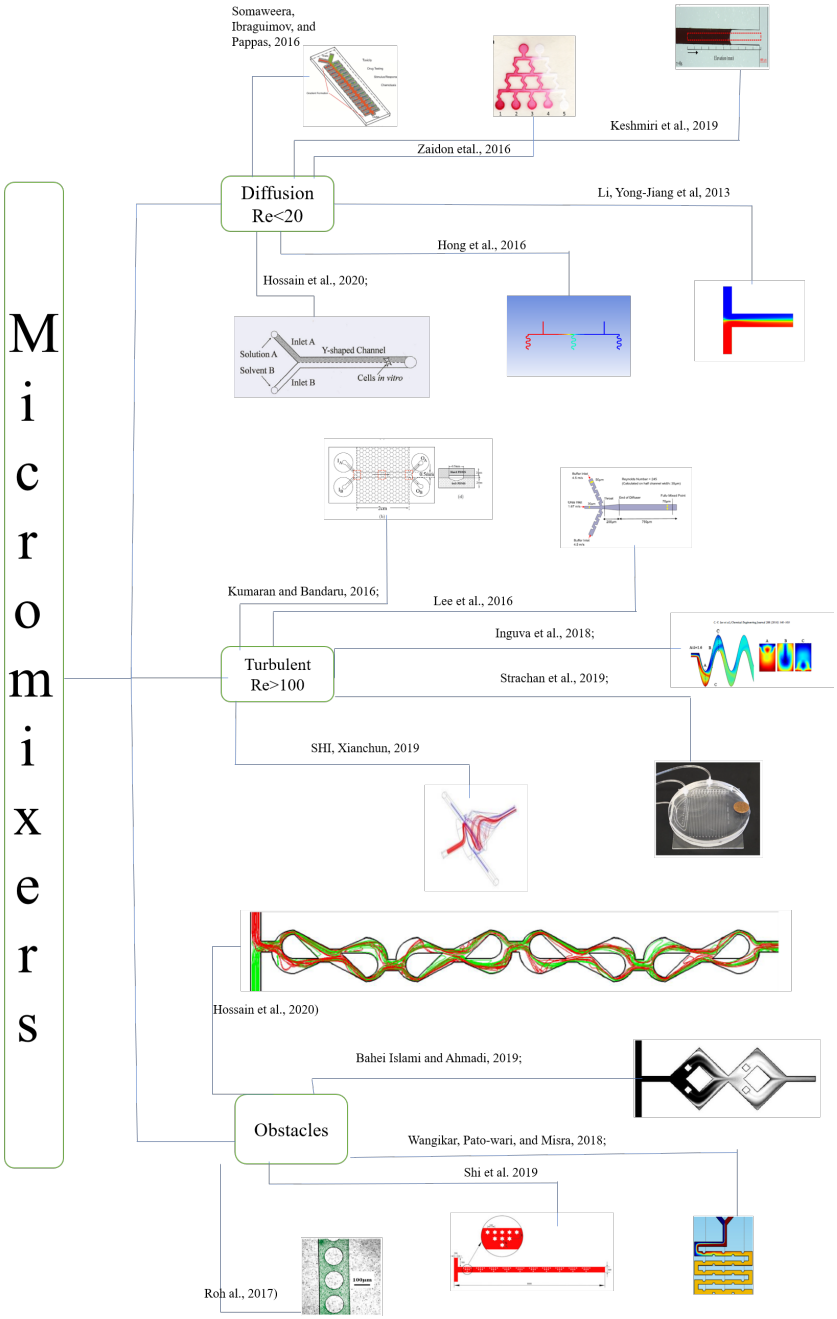

FIGURE 1.9: Micromixer devices developed in the recent years and acting throughturbulent flow, obstacles mixers and diffusion phenomenon.

Table 1.2 discussed in detail the microfluidic devices showed in Figure 1.9. For example, more details about Re, geometries, fabrication technique and application. The involved mixing process is presented in terms of the physical and geometrical properties for whatever scale, geometry shape, fluid properties and velocity of the fluid.

Even these micromixers are called **passive micromixers**, they need an external energy pump to produce fluid flow into the microchannel. There are different external pumping methods with a variety of operating principles such as: mechanical and non-mechanical pumps (Nguyen, Huang, and Chuan, 2002); for example, the **gravity pump** can be classified such as non-mechanical pump. On the other hand,

the most required is mechanically managed where a motor push a syringe with the fluid of interest; the last one was used in this thesis work. This becomes important because, same microfluidic devices (geometry, scale, shape) with same involved fluids can support the two discussed flow regimes: the laminar and the turbulent. This will be better explained in the next subsection throughReynolds number which directly depends on the velocity of the fluid and the device geometrical aspects.
From Table 1.2, it can be notice that the fabrication of microfluidic devices, for this particular case: micromixers, generally range from UV-photolithography procedures based on masks to direct writing protocols. The fabrication of devices based on photolithography normally requires the use of clean room facilities which represents expensive fabrication machines. On the other hand, fabrication protocols based on direct laser writing go from the use of expensive laser source to very cheap ones such as optical pointers. This work is based on the latest experimental feature where all the presented devices were developed by using a low cost CW-laser and patterned through a home-made 3D opto-mechanical platform. The use of DLW fabrication protocols, in addition, represents a unique opportunity in terms of 3D designs and easily achievable simple and complex microfluidics designs.

Reference	Mixing Process	Involved Geometry	Re	Fabrication Technique	MicromixerApplication
(Somaweera, Ibraguimov, and Pappas, 2016)	Diffusion	serpentine	<20	Paper-based lith.	chemical gradient
(Zaidon et al., 2016)	Diffusion	serpentine	<20	—	simulation
(Keshmiri et al., 2019)	diffusion	T-shaped	<20	UV Mask	Diffusive mass transfer
(Dauyeshova, Rojas-Solórzano, and Monaco, 2018)	Diffusion	T-shaped	<20	—	simualtion
(Li et al., 2013)	Diffusion	Y-shaped	<20	Buy it	Cells in-vitro .
(Hong et al., 2016)	Diffusion	serpentine	<20	UV mask l	cell culture
(Strachan et al., 2019)	Turbulent F.	Y-shaped	50	Polymer cat.	cell culture
(Strachan et al., 2019)	Turbulent F.	Zig-Zag	>20	Photo-MAsk	cell culture
(Lee et al., 2011)	Turbulent F.	Zig-Zag	$\tilde{1}00$	UV mask	simulation
(Inguva et al., 2018)	Turbulent F.	Y-shaped/obstacles	$\tilde{2}50$	—	simulation
(Kumaran and Bandaru, 2016)	Turbulent F	double y-shaped	$\tilde{5}0$	Polymer Catalysis	Chemical R.
(Shi et al., 2019)	Turbulent F.	3D vortex	$\tilde{5}0$	—	simulation
(Bahei Islami and Ahmadi, 2019)	obstacles	single channel	<1	—	Mixing degree Sim.
(Wangikar, Patowari, and Misra, 2018)	obstacles	serpentine	«1	—	simulation results
(Shi et al., 2019)	obstacles	Koch array	0.28	UV Mask technique	passive micromixer
(Wangikar, Patowari, and Misra, 2018)	obstacles	serpentine	0.28	Mold Lithography	Micromixer
(Hossain et al., 2020)	obstacles	Tesla structure	100	—	simulation
(LaFratta et al., 2015)	Diffusion	Y-zag shaped	—	DLW S-L	Micromixer
(Lim et al., 2018)	—	Zag-cuted	—	DLW S-L	—
This Thesis Work	Diffusion	Y-serpentine shaped	9.17	DLW	Micromixer

TABLE 1.2: Microfluidic devices employed as micromixers.

Table 1.2 shows in detail the parameters, Re and application of the state of the art on micromixers. Here, it can be observed the different phenomena discussed above and how the Re and the geometry influences directly into the final applications.
As has been mentioned above, to achieve a mixing process (in macro and micro scale) it is necessary categorized the type of fluid flow that, it is presented in the systems according to the characteristics of the mixer, the physical properties of the involved fluids and their fluxes.
In microfluidics, the flow of fluids through microchannels is usually laminar flow (Groisman and Quake, 2004). Laminar flow is associated with flow-streamlines that are both well oriented and well positioned along the microchannel at whatever time and whatever point along the device. While those that are not laminar, are classified such as turbulent, with streamlines that are not more well-oriented and individual positions of the flow (considered that the flow is supported by individual particles where each one has a coordinate) that are randomly-oriented. There exists a position where these two regimes appears which is commonly refereed such as flow-transition (Wang, Yang, and Zhao, 2014). Figure 1.10 is an artistic representation of the discussed above.

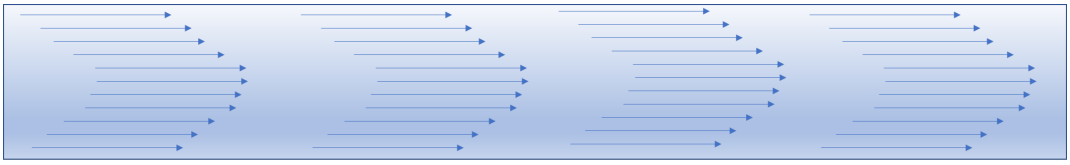

Laminar Flow Regime

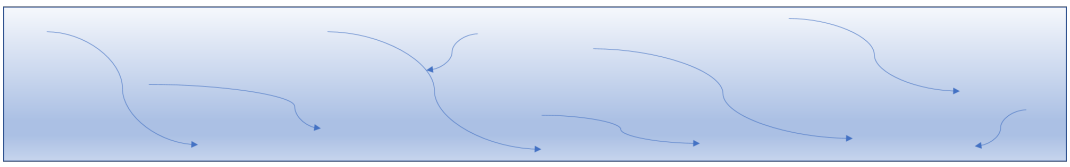

Turbulent Flow Regime

FIGURE 1.10: Comparison between the laminar and turbulent flow in streamlines.

The physical quantity that describes the fluid flow regime is the Re and can be deduced from the Navier-Stokes equation as it was observed in the previous section, Re and the fluid flows regime involved are presented in Table 1.3

Reynolds number	Regime	Scale
<2300	Laminar	Macro-scale
2300>Re<2900	Transition	Macro-scale
>2900	Turbulent	Macro-scale
<20	Laminar	Micro-scale
>100	Turbulent	Micro-scale
20>Re<100	Transitions	Micro-scale

TABLE 1.3: Re number-classification

1.6 The diffusion equation

Diffusion is an statistical phenomenon at the molecular level which is caused by random motion of the molecules. At the macroscopic scale, the diffusion phenomena is generally not as important as at the microscale, particularly, at this level, this can give a significant contribution to the transport of matter. Diffusion phenomena is described by the Fick's first law(Bruus, 2008):

$$\vec{J_{dif}} = -D\vec{\nabla}c \tag{1.10}$$

Fick's law describes, in the solute, the motion of a diffusion current density $\vec{J_{dif}}$ is directed toward those regions of low concentration density c. Here D is the diffusion coefficient associated with the solute. Using the continuity equation for flux and concentration:

$$\frac{\partial c}{\partial t} + \nabla \vec{J_{dif}} = 0 \tag{1.11}$$

By considering equation 1.10 and substituting in equation 1.11it is possible to obtain the Fick's second law

$$\frac{\partial c}{\partial t} = D\nabla^2 c \tag{1.12}$$

This last equation describes how the concentration change with the time, according with the diffusion coefficient of molecular species and the initial c. The diffusion phenomena is a NL process in which, the time t required for a species to diffuse scales quadratically with a the length-scale **x** and it can be defined as the process of spreading molecules by random motion from regions from higher concentration to those with lower concentration. The diffusion coefficient in this way can be expressed as:

$$D = \frac{x^2}{t} = \frac{\kappa T}{6\pi\mu R} \tag{1.13}$$

This expression is derived from the Einstein-Smoluchowski equation (for very low Re) where **T** is the temperature (K), μ the viscosity of the medium ($\frac{Ns}{m^2}$), **R** (m) is the radius of the particle or molecules (Capretto et al., 2011) and **K** the Boltzmann constant ($\frac{Nm}{K}$) becomes important because shows that the diffusion phenomena depends directly of the **T** and **R** which must to be considered in the experimentation. Both expression relate the mobility of particles in a certain scale so in a microscale the diffusion distance can be very small due **x** varies quadratically and the time required to complete mixing is reduced dramatically, then the microfluidic systems are able to mix particles or molecules by only diffusion phenomena. When a fluid flow is considered in a micro-scale and the Re is small enough to guarantee the laminar flow, 1.2, the mixing process is entirely dominated by diffusion and the time to complete the process is dramatically reduced given the Equation 1.13. If an specific concentration of a solute circulates along the microchannel this is dependent of both the position and the time. In this way a solution of 1.12 has the form (Bruus, 2008):

$$c(\mathbf{r}, t > 0) = \frac{N_0}{(4\pi D t)^{\frac{3}{2}}} e^{\left(\frac{-r^2}{4\pi D t}\right)} \tag{1.14}$$

Taking the equation 1.13 and 1.14 the Figure 1.11 shows a time evolution according to the length-scale and how the concentration changes along the distance given

an specific diffusion constant D=$2x10^{-9}m^2s^{-1}$ that correspond to the Rhodamine B (Gendron, Avaltroni, and Wilkinson, 2008).

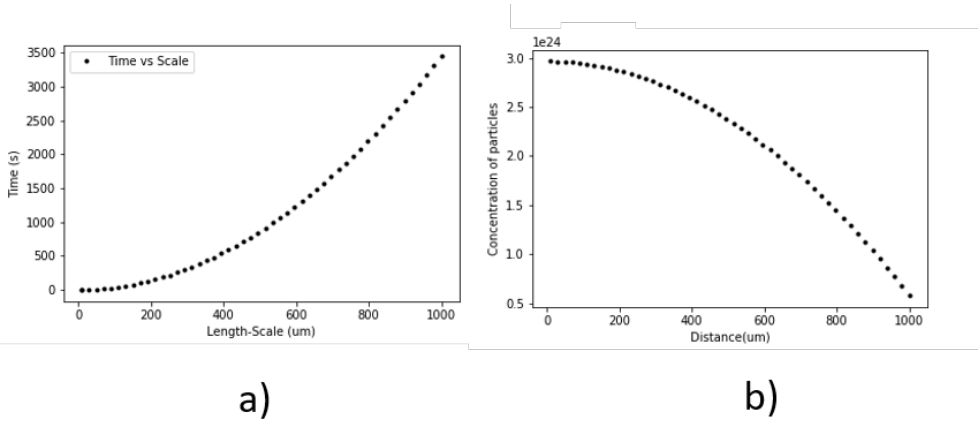

FIGURE 1.11: a) Evolution in the increment of time with the increment of scale and b) how decrease the concentration with the length scale.

For the micromixers system, the surface contact area and the mixing path are usually the two main points to design geometries of channels at the microscale. Those geometries are typically the T-shaped, Y-shaped, focusing mixers, microdroplets (Lee et al., 2016) mixers and others . Those geometries are considered as passive microfluidics systems because they not use an external force to produce the mixing. In this thesis work we focus our attention in two micromixers geometries a simple Y-shaped and serpentine Y-shaped micromixers.
Active micromixers usually have a higher efficiency of mixing, compared with the passive micromixers, but its employment and execution is generally very complicated and with a high cost, the type of external forces used in this kind of micromixers are ulstrasonic-driven, magneto-hydrodynamic or temperature induced mixing and pressure field driven (Nguyen and Wu, 2004).

Chapter 2

Fabrication of Master Mask for Micromixer Devices

In this chapter the protocols and methodology for the three fabrication steps are described. The variation of different experimental parameters (doses) and procedures employed in each engraved structure are presented and described. To fabricate the polymerized master mask, a complete fabrication protocol was developed, this includes from the appropriate cleaning and the dehydration of the SLG to the treatment after the laser exposure. As mentioned before, the fabrication of polymeric microstructures was done through DLW protocols. In addition, before laser exposure, others specific fabrication steps were required, for example, a homogeneous film deposition of the photoresist over a thick soda lime glass substrate (SLG), this issue is important to ensure homogeneous thickness.

2.1 Photoresist Deposition Method

To ensure a homogeneous deposition of photoresist on the SLG, normally a spin coating method is used (Keller et al., 2008). This method is simple and ensures the homogeneity on the final photoresist layer thickness. In the state of art, photoresist with very low to moderate viscosity property (14 to 65 cSt) are ideal to be used for this method. Problems arise when the photoresist becomes more viscous (4500 to 22000 cSt), in the particular case of SU-8 (12700 cSt), the spin coater does not ensure a uniform distribution of the layer; thus, an alternative film deposition method must be considered for this. The drag method can, in this way, achieve a well-accepted homogeneous layer.

In the drag method, fully implemented in our laboratories, a knife is automatically controlled by a linear translation platform. The z-positions of the knife is, in addition, manually controlled by a micrometer stage to achieve the desired photoresist thickness with a resolution of $25\mu m$, the minimum mechanical step of the platform.

The procedure starts by depositing SU-8 on a SLG and placing them in the automated platform (see Figure 2.1), to achieve the desire thickness the knife is in contact with the SLG (without SU-8), by using this position as the zero, then the micrometer platform is carried up for an specific distance.

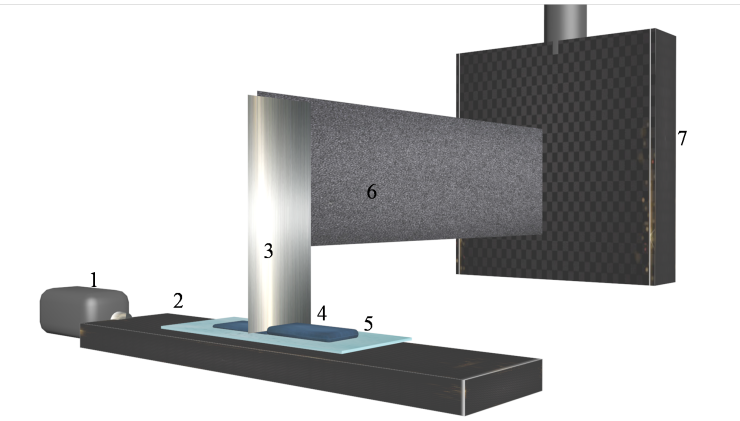

FIGURE 2.1: Artistic representation of the deposition: stepper motor, 2: linear platform, 3: knife, 4: SU-8 deposition, 5: SLG substrate, 6: knife holder and 7: manual micrometer stage.

The knife spread the photoresist along the SLG substrate where the thickness was previously configured by a micrometer. The speed on the deposition procedure was controlled automatically and chosen to be 400 μm/s. In addition, the film deposition was constantly monitored by an USB micro-camera. Previously to the photoresist deposition, the SLG is first properly cleaned by using a bath of acetone (5min), isopropanol (5min), distilled water (5min) and dehydrated at 65° C (5 min) to eliminate any possible residual solvent. By following this deposition procedure, it is possible to achieve layer thickness that range from 25 μm to 200μm, Table 2.1.

2.2 Fabrication of the master masks

The microfluidic devices are manufactured by following the next main fabrication steps: 1.- The fabrication of the master masks by DLW based on LOPA protocols. 2.- The fabrication of the microchannel through soft-lithography procedures. 3.- The conformation of the microfluidic chip by plasma bonding procedures.

The step 1 considers all the phenomena above explained. The main geometries of our devices will be based on Y- and Y-serpentine shaped trajectories. The design of these patterns were carried out through LabVIEW software which also control the 3D mechanical platform.

For the master mask fabrication, the Figure 2.2 shows the general procedures involved in the manufacture which ranges from the cleaning of the SLG to the final hard-baking. To fabricate a well contoured pattern, a special thermal treatment is recommended. Briefly, the pre-baking ensures eliminating any residual solvent while the post-baking process (PEB: Post Exposure Bake) improves the polymerization of the exposed SU-8. Finally, the hard-baking is widely used to boost the sticky condition between the polymerized SU-8 and the SLG (Parida and Bhat, 2009; MICROCHEM, 2017)

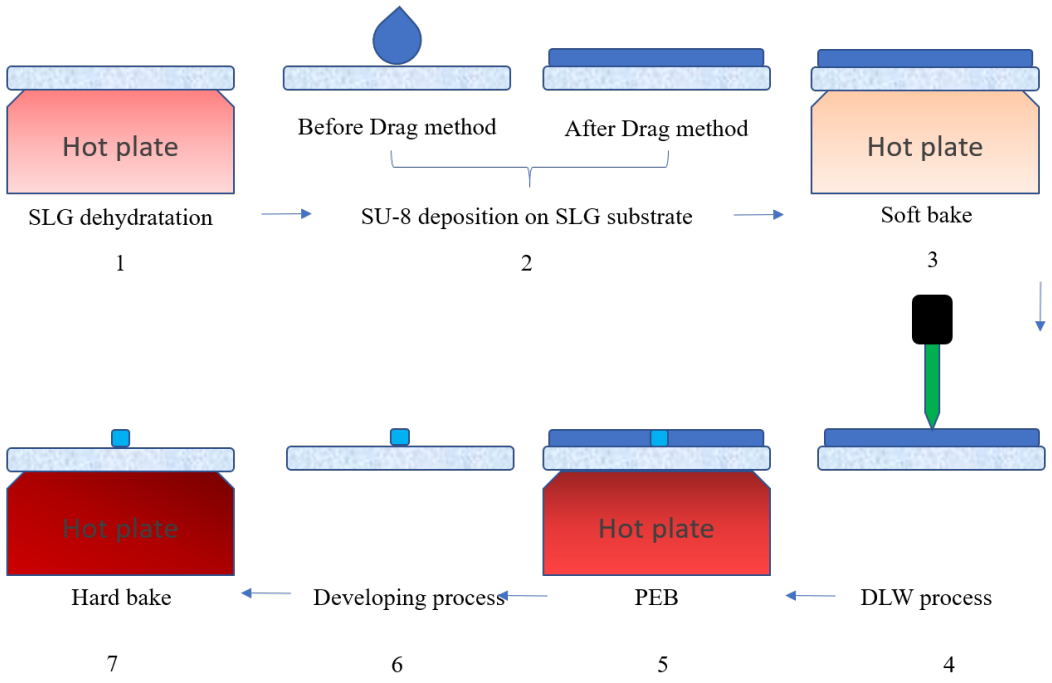

FIGURE 2.2: Fabrication protocol steps 1.

From figure 2.2, the deposited film is placed on the three dimensional platform (3DP) where the patterns are transmitted, here, the photo-polymerization is achieved by moving the sample along the focused laser radiation, details are shown in table 2.1. After laser exposure, the sample is placed on a hot plate for 12 minutes. During this time, the polymerization process is totally completed and the irradiated area turns to solid. After that, the sample is placed in a SU-8 developer bath which takes between 15-20 minutes depending on the deposited SU-8 amount. In this step, the non-polymerized photoresist is removed. Finally, the fabricated structure is moved back on the hot plate, for the final hard-baking treatment to avoid the detachment of the polymerized structures when it is employed as a master mask.

Step	Time (min)	Temperature (°C)
SLG dehydration	5	65
SU-8 deposition on SLG substrate	—	—
Soft bake	2	65
DLW process	—	—
PEB	12	95
Chemical reveled process	20	—
Hard Bake	30	150

TABLE 2.1: Microstructures Fabrication Protocol

The most relevant results obtained in terms of mask fabrication are presented in Figure 2.4. Besides the protocol presented in Table 2.1, the laser exposure requires a global experimental comprehension in terms of light-matter interaction. First, the intensity dependence was investigated. Different micro-lines were fabricated by using a 10X MO with NA= 0.25, varying the intensity laser radiation from 12 to 130 mW in steps as shown in Table 2.2. In same way, by varying the focal distance, different printing conditions can be achieved in terms of diameters and dimensions.

Even though the resolution of the spot is governed by the Rayleigh criteria, it is possible to increase the polymerized area (PA) by simply increasing the intensity power and/or changing of the microscope objective position (z-axis) from its work distance (WD).

Doses	PA (μm)	Intensity (mW)	Focal Position(mm)	V ($\mu m s^{-1}$)	Repetitions
ω_0	50	12	WD	5	1
ω_1	90	12	WD	200	40
ω_2	110	20	WD	400	40
ω_3	500	110	WD+3	400	40
ω_4	700	120	WD+4	400	40
ω_5	800	130	WD+5	400	40

TABLE 2.2: Polymerization area achieved by the variation of the presented doses.

As discussed above, by following the doses showed in Table 2.2 it was possible to fabricate different polymeric microstructures. Figure 2.3 shows the experimental setup used to fabricate the master masks. In this, it is possible observe the CW laser source, optical devices, external power source for the Drivers, 3DP, home-produced software and the electronic devices to achieve the polymeric microstructures fabrication. The experimental platform was fully designed, fabricated and implemented in our laboratory with many technological purposes such as microfluidic and photonic applications. Details of the experiments can be founded elsewhere (Camarena-Chávez et al., 2020)

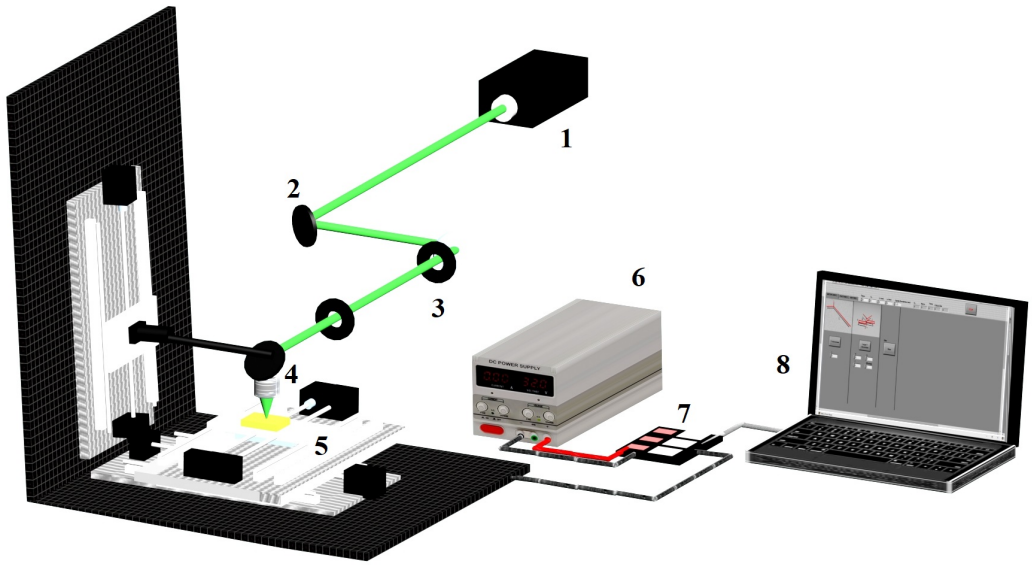

FIGURE 2.3: Experimental setup for microfabrication LOPA based DLW. **1**: CW 532 nm laser, **2**: mirror, **3**: iris,**4**: Microscope objective,**5**: three axes platform,**6**:external power supply, **7**: Arduino-SM drivers connection and **8**: developed LabVIEW software to control the 3DP.

Before selecting the corresponding doses, according to the application, and following the protocol described above, many master masks were developed, with the aim to demonstrate the utility of the 3DP and the corresponding experimental setup

microfluidic chips were developed from the master masks. Figure 2.4 shows a collection of master masks fabricated, its details and application will be discussed in the next chapter. It can be observed that the PA increases with the variations mentioned above. The PA change from 50 to 833 μm. From this, it is observable that under different exposure laser doses, different sizes, heights and qualities are achievable. For the fabrication of micro-channels using only one of the linear platform with constant and well-defined height, no defects were observed, however, in the combined moving of two linear platforms, some defects appear and can be associated with the combined backlash in the system, which is inherent to the mechanical devices, Figure 2.4 e). The different shapes presented in Figure 2.4, particularly b), c) and d) represents the potential applications of this printing protocols to several technological projects such as b) biosensors based on microchannel c) particle selectors and optical fibers and d) finally label-free sensors based on photo-acoustic protocols.

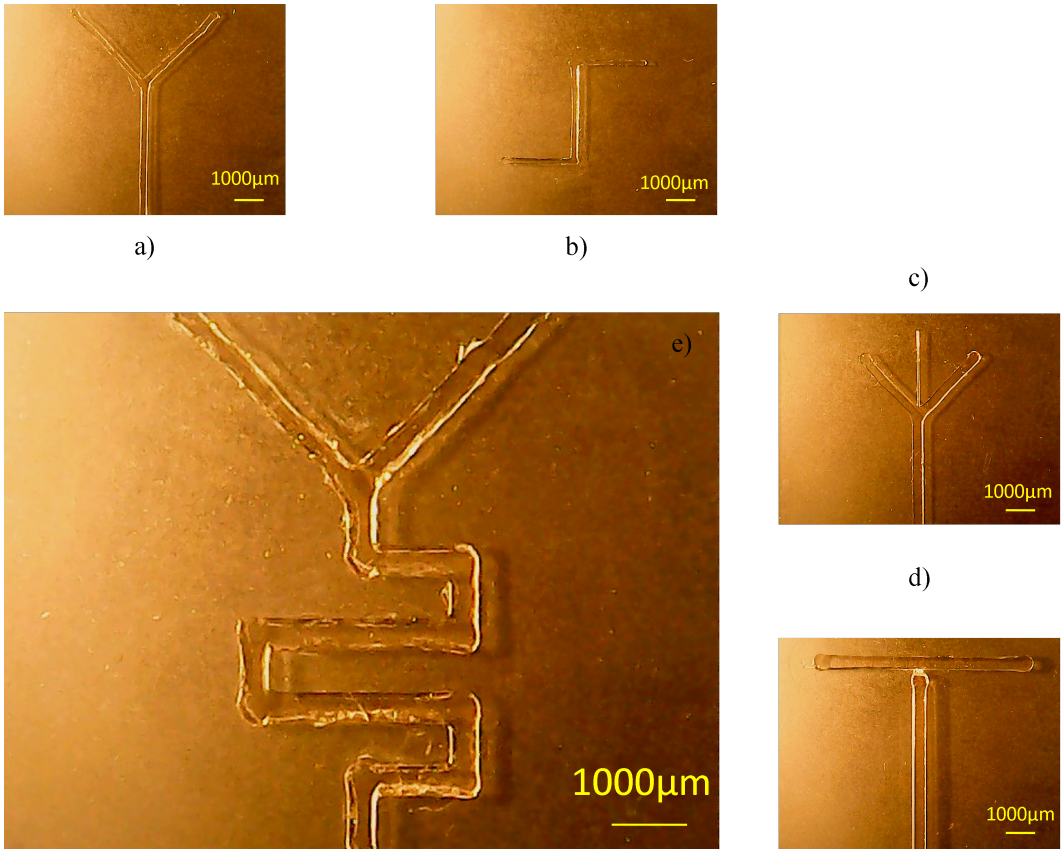

FIGURE 2.4: **a)** The simplest Y-shaped geometry for a micromixer, **b)** z -shaped master mask to use in a waveguide sensor, **c)** master mask to be use as clogging-free microfilter, **Tcut-shaped** master mask, to fabricate a microfluidic-photoacoustic device and **e)** serpentine-shaped master mask.

The master masks showed in Figure 2.4 are not the microfluidic systems yet, to do that, they must pass to other widely employed techniques: soft-lithography and plasma surface.

2.3 Soft-Lithography Technique and Bounding Process

After the DLW based LOPA fabrication the master masks were underwent to the soft-lithography process, applying the protocols widely reported (Kim et al., 2008). This protocol consists in the fabrication of a negative form from the master mask. For this thesis work, a commercial silicon-based organic polymer called polydimethylsiloxane (PDMS) was used for the development of the microfluidic devices. It is previously demonstrated that the PDMS reproduces the master masks forms at nanoscale resolution which represents a potential fabrication procedure to scale applications at this size (Mata, Fleischman, and Roy, 2005). Figure 2.5 shows the general steps to create negative molds from master masks.

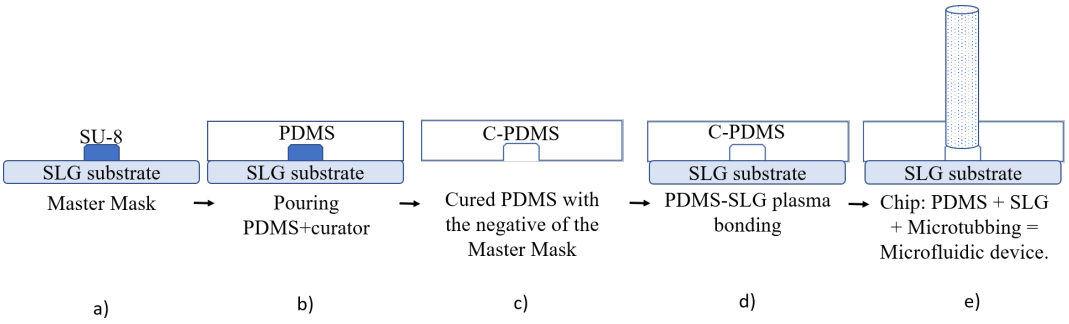

FIGURE 2.5: **a)** presents the fabricated master mask where is poured the **b)** PDMS and by through a baking process, **c)** this is curated and finally obtained with the negative of the master mask, after that the **d)**: the superficial plasma treatment allows the chemical bounding along both: the silica substrate and the PDMS to obtain a **e)** microfluidic device.

Initially, the PDMS base is a viscous polymer, after being mixed with methyltrichlorosilane (curator) the crosslinked process can be accomplished by two options, the first one is after 24 hours at room temperature or, the second one, after 1.5 hours at 110 °C, in this thesis work the first option was used because it is possible to avoid forming bubbles during the full process which takes 24 hours. After the cross-linked process, the C-PDMS underwent to a plasma bonding process, in which, the C-PDMS is glued to a SLG substrate via surface activation as it is shown in Figure 2.6, the scheme presents how the chemical process is carried out by plasma activation. The activated surfaces of the SLG and c-PDMS were brought into contact producing covalent bonds, forming the microfluidic chip.

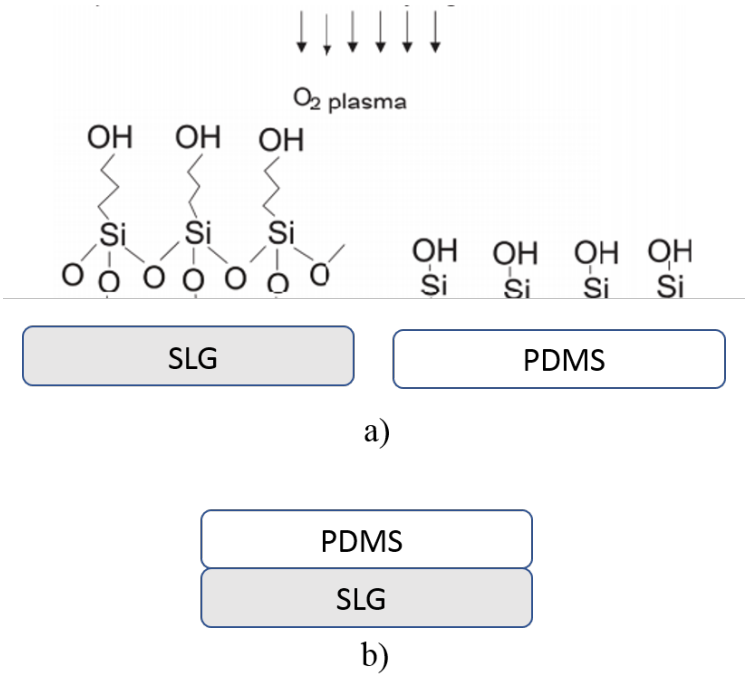

FIGURE 2.6: Plasma bonding a): Formation of silanol groups on the SLG substrate and the PDMS surfaces by oxygen plasma treatment, b): PDMS/SLG brought into contact forming a sandwich covalent bonding.

Briefly, the PDMS base is mixed with the curator in a proportion of 10:1, then, the mixture PDMS-curator is poured over the master mask and subjected to a baking process where the PDMS and the mask are put it to rest in a horizontal position during 24 hours, immediately after the crosslinked process is completed, the PDMS turns from liquid to solid (C-PDMS) to finally separate the C-PDMS from the master mask to visualize the microchannels. Before initializing the bonding treatment, the C-PDMS was perforated to produce the tubing inlets and outlets, this was carried out by a biopsy punch with a diameter of 1 mm.
The main mechanical and optical properties of the engraved C-PDMS, are respectively the density of 965 kg/m^3 and refractive index of η=1.4.

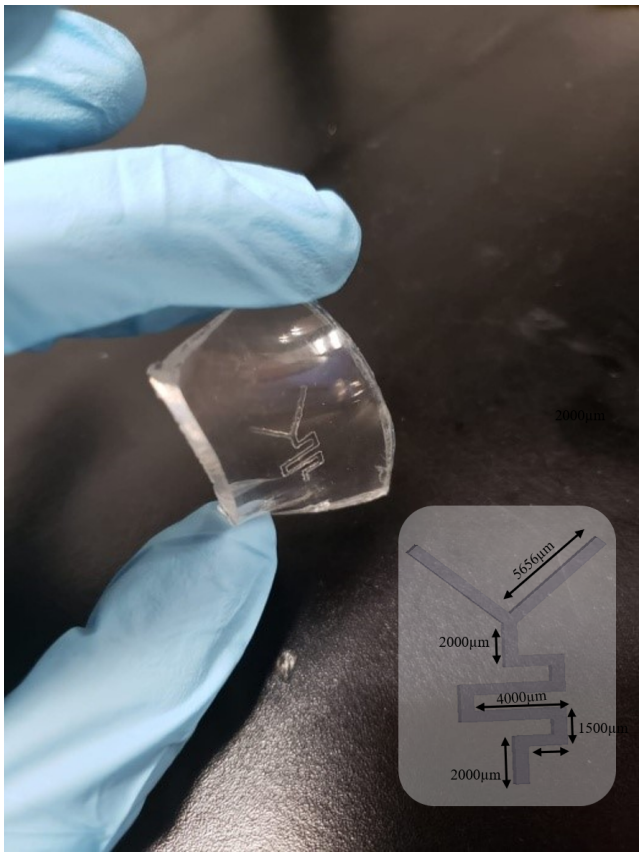

FIGURE 2.7: Serpentine-shaped micromixer achieved on the C-PDMS surface, it can be observed the elasticity and translucent characteristics of the curated PDMS (C-PDMS).

Figure 2.7 shows how the C-PDMS looks. It is shown that the master masks pattern was accurately transmitted to the PDMS through soft-lithography procedures. This picture demonstrates that in our lab and under the discussed fabrication procedure we have the experimental condition to both fabricate master masks with complex pattern and to follow soft-lithography procedures to develop high performance C-PDMS. The inset in figure shows the render with the complete description of its geometrical parts.

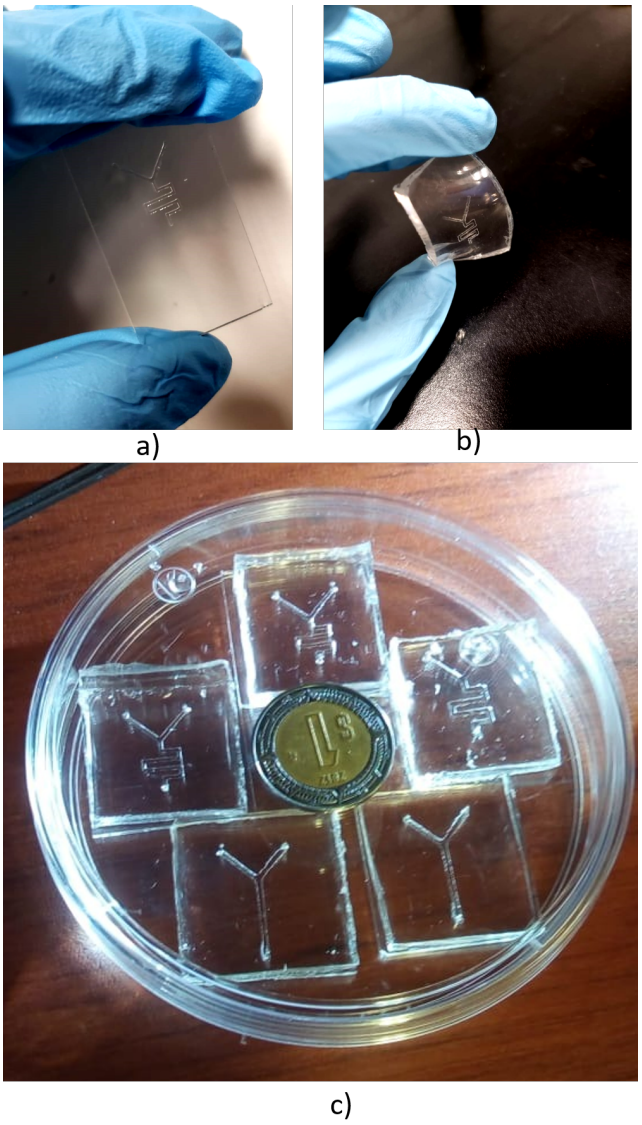

FIGURE 2.8: Pictures of the **a)** serpentine-shaped master mask fabricated with the parameters described for ω_2, **b)** negative mold of the C-PDMS and **c)** micromixers devices after the bounding process, it is possible observe the hole pipe in both: inlets and outlet.

The microfluidic chips are finally presented in Figure 2.8. From all of them, it is highlighted that the master mask patterns were well transmitted to finally achieve the microfluidic chips. Once the master mask is developed, the pattern, in addition, can be transferred as many times as the final users require as presented for the micromixer based on Y-serpentine shape.

Chapter 3

Results for Micromixer Devices

In this chapter, the application of microfluidic chips, finite element method simulations, the experimental techniques to characterize them, the compiled data from fluorescence spectroscopy and the comparison between experiments and simulations are presented. The finite element method simulations were carried out through COMSOL Multiphysics software. In addition, the global steps to communicate with COMSOL to achieve micromixers based on microfluidic devices are presented in detail.

3.1 Simulations based on COMSOL Multiphysiscs

Before initiating the experimentation, fluid simulations of both Y-shaped and serpentine-shaped were carried out. Because both geometries work such as micromixers, simulations allowed us to discern the most effective configuration. The material and fluid flow properties implemented in the simulations are presented in the Table3.1.

Sample	D (x$10^{-10} m^2 s^{-1}$)	μ (Pa*s)	Caudal (ml/min)	$\rho(kg/m^3)$	ReN
RB	2.9	90	0.05	0.797	9.726580
Methanol	2.3	110	0.05	0.796	9.723756

TABLE 3.1: Fluid properties used in the simulation.

By considering parameters from Table 3.1 and implementing the geometrical and spatial device characteristics from the corresponding master mask, the Y-shaped and Y serpentine-shaped were simulated as micromixers. Figure 3.1 shows in detail the involved steps in COMSOL simulation.

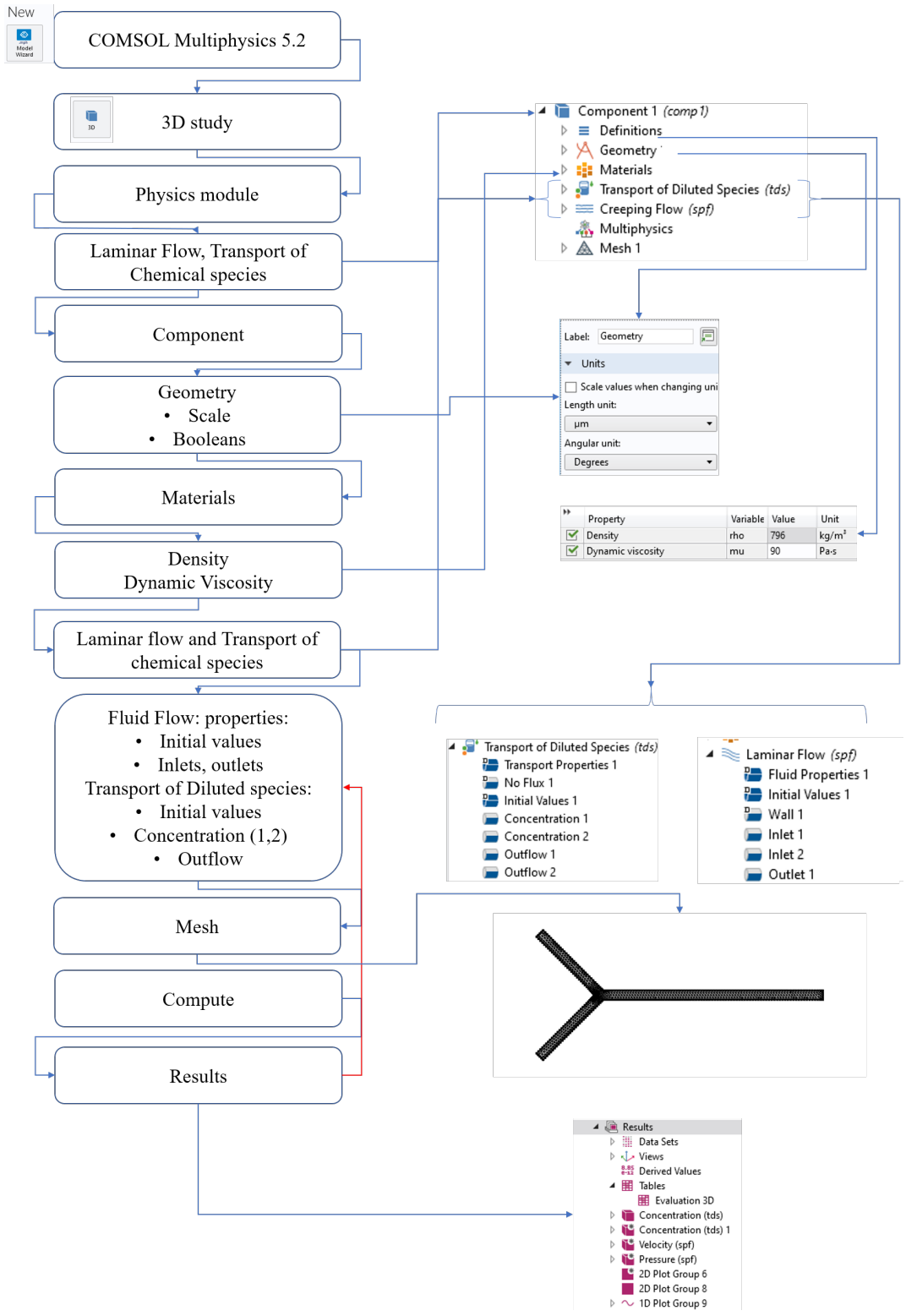

FIGURE 3.1: Schematic diagram to create a COMSOL simulation

The COMSOL simulations begins defining the **physics module** which will be implemented in a 3D study. In microfluidic devices, the **laminar flow** module is mandatory. Because the microfluidic systems are applied such as micromixers, the **Transport of chemical species** is added in the study. The geometry is designed in the component section, the design starts in a plane work (2D design) where the volume

is extruded to create a 3D geometry domain. Once the design is finished, the material properties are defined. Because RB is used as the chemical compound to mix with methanol, this is defined for each selected inlet. In the **laminar flow** section, the inlets and outlets are defined in the geometry and for the **Transport of chemical species**, the initial concentration in the inlets are established. Once these steps are completed, the immediately next one is to compute simulations. The stationary study is implemented, which solve the concentration gradient of RB along the microchannel in the simulations. The results allow us to estimate the mixing spatial evolution along the channels, moreover, the pressure, velocity, vorticity and the resulted data are all available for an extra analysis.
As an example, Figure 3.2 shows the mixing evolution simulation for the two different geometries through the integrated concentration gradient instruction. The scale bar represents the concentration value, in Mol/L along the microchannel. Going from red to blue where the inner colors (green-yellow) show the efficient mixing process. The concentration gradient is presented for both devices. We can immediately discern that through the Y-shape geometry, we have lower opportunity to achieve a full species mixing as happens through the Y-serpentine geometry where the mixing process is fully achieved at the last part of the device (visually observable). The phenomenon that governs in both simulations is the diffusion process; laminar flow was kept for both devices. From Figure 3.2 a), the mixing process begins in the interface between both fluid and it is achieved by diffusion generating a gradient concentration, which is carried out from region of low concentration (blue) to region of high concentration (red) until the full mixing of fluids (green).

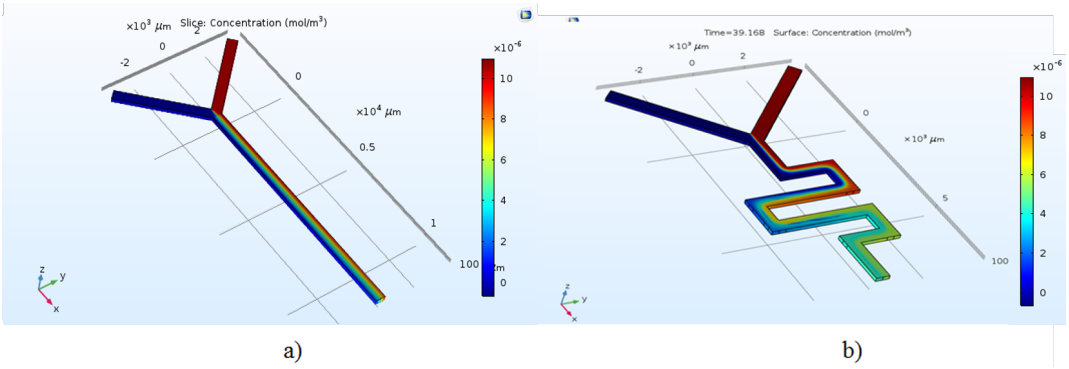

FIGURE 3.2: a) The y-shaped micromixer and b) shows simulation for the Y serpentine-shaped micromixer. In this figure it can be observed the mixing process along the respective channels.

The evolution on the concentration range from $1x10^{-5}$ Mol/L to $5x10^{-6}$ Mol/L after been mixed with methanol. The best result of mixing, under the same material properties, was the device based on Y serpentine form. This geometry shows the complete mixture between the fluids so, as a conclusion, the Y-serpentine shape is presented as an ideal device to achieve the mixing of chemical species. For the scope of this thesis work we will present the functionality and versatility of this device for the mixing of RB and methanol.

3.2 Micromixers

In this section, the application and discussion of the obtained results from the microfluidic chip with Y-serpentine shape are presented as well as the Experimental

details and employed equipment.

With the aim of demonstrating the functionality of the device, different dye fluid concentration measurements were done through fluorescence spectra acquisition. Seven different aliquots under study were prepared. To characterize the molar concentration evolution, through fluorescence microscopy, the microfluidic chip was optically excited in specific areas along the microchannels, Figure 3.3

3.2.1 Micromixers Results

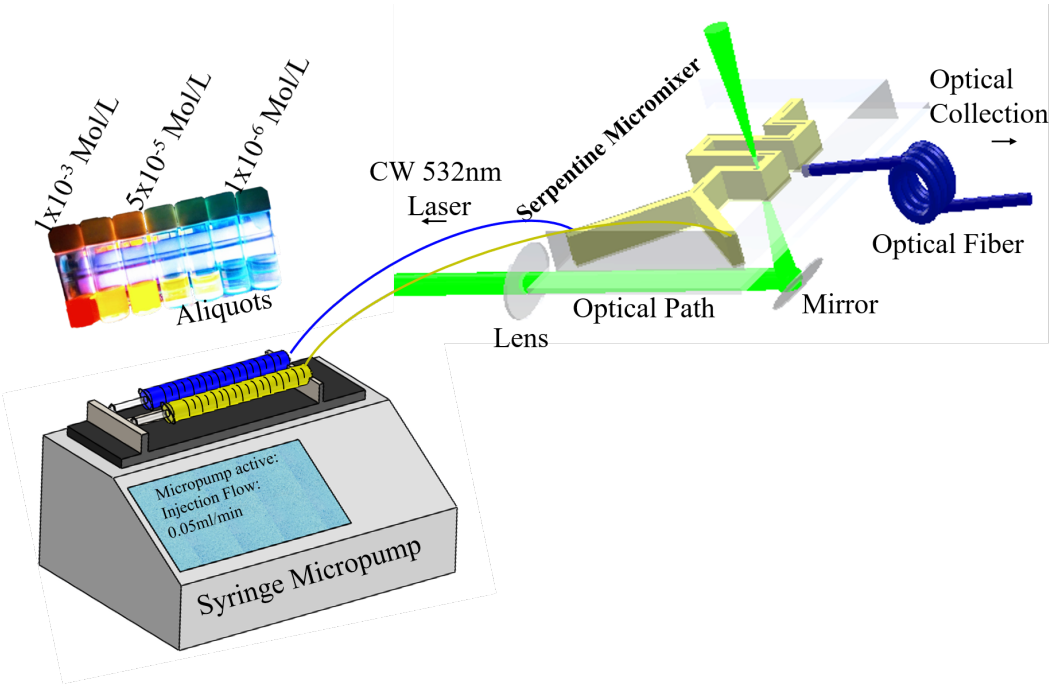

FIGURE 3.3: Artistically representation of the experimental setup the micropump , syringes the micromixers device and in the inset the corresponding aliquots of RB are showed .

Figure 3.3 shows the aliquots concentrations: from left to rigth:$1x10^{-3}$,$5x10^{-4}$, $1x10^{-4}$,$5x10^{-5}$,$1x10^{-5}$,$5x10^{-6}$ *and* $1x10^{-6}$ Mol/L. Because the aliquots are based on a fluorescence material (RB), once laser optically excites whatever of the selected areas along the device, fluorescence emerge in all directions. The corresponding fluorescence emission was collected throughan optical fiber which was connected to a spectrometer analyzer (Ocean Optics 3000 series). The relative positions between the micro-mixer device and the optical pump remained unchanged ensuring the same intensity levels for the full set of measurements.

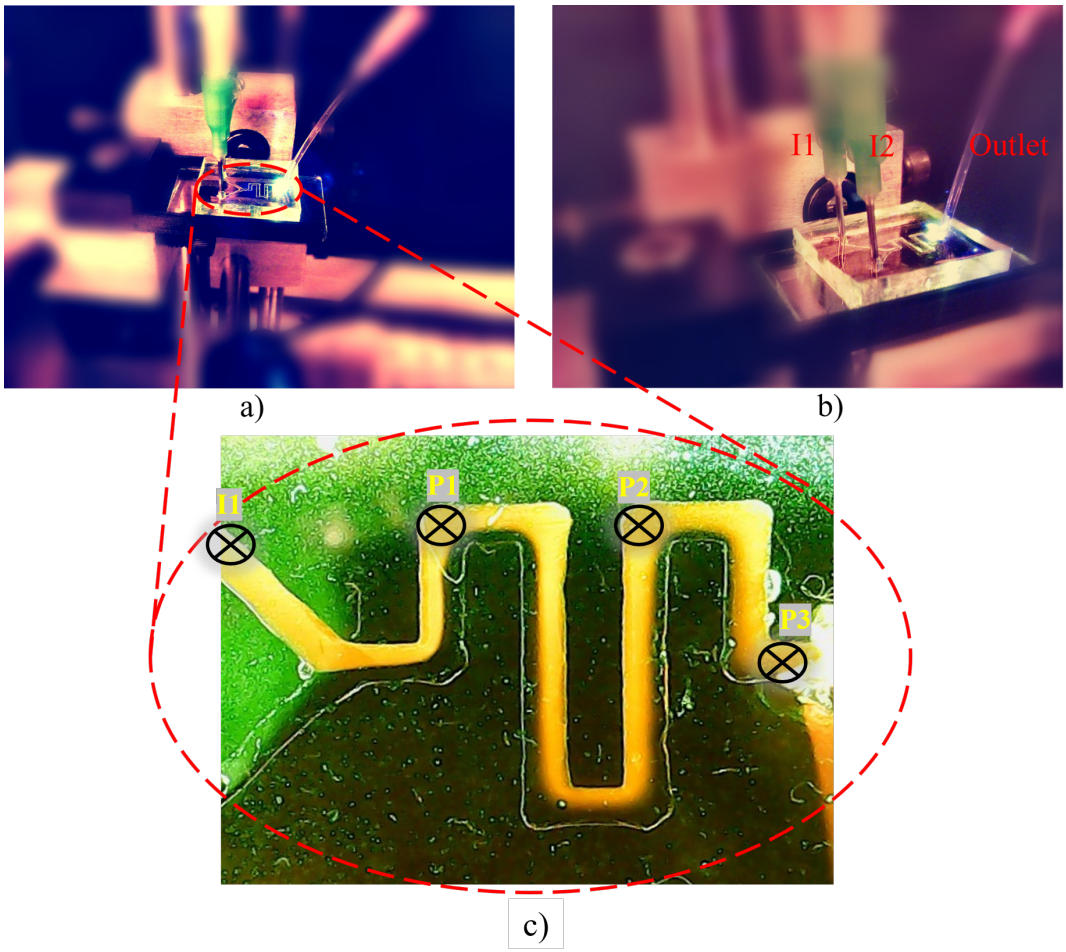

FIGURE 3.4: **a)** and **b)** photos from the experimental setup, zoom to the microdevice, I1 is the inlet for the RB and I2 for the pure methanol. **c)** Picture acquired from a microcamera during the experiment,the fluorescence is achieved by pumping wit a CW laser at 532nm, the measured points are marked.

A set of highlighted images of the device and the points under study are shown in the Figure 3.4. The molar concentration variation monitoring was done by considering four localized positions in Figure 3.4 c), two at the inner part and the other two at the inlet and outlet. From the state of art, (Fang et al., 2011), (Chabinyc et al., 2001) and (Hübner et al., 2001), carried out fluorescence microscopy analysis to follow variation in the concentration on molecular species mixed and measured through microfluidic chips. This is achieved by pumping fluorescent dyes or molecules into microfluidics channels and mixing with no fluorescent buffer, because a diffusion gradient concentration is induced along the mixing channel which, in addition, produce a change in the amplitude intensity of the mixture. The acquisition of fluorescence measurement were proposed to be accomplished by fiber optics (Hübner et al., 2001; Chabinyc et al., 2001), or by digital image processing (Parittotokkaporn et al., 2019), whatever the employed method, the main idea is relating the maximum fluorescence amplitude with an specific dye concentration, and compare this, with the fluorescence emission of the mixed dye. For these cases, a linear behavior between the dye concentration and the fluorescent intensity along the mixing channel fluorescence intensity has been reported.
In this thesis work the fluorescence emission from the mixing channel was collected

using an spectrometer **via** an optical fiber. The optical fiber position was set perpendicular to the device as presented in Figure 3.3 and oriented where the P1, P2 and P3 points are highlighted.

With the aim to calibrating the microchip, the aliquots fluorescence intensities were acquired in I1. As exposed by (Fang et al., 2011) and (Hübner et al., 2001), the calibration curve from the acquired data, which is developed between intensity and concentration, is expected to be a linear which facilitates a reliable quantification. The 7 concentrations were used to develop this curve, Figure 3.5.

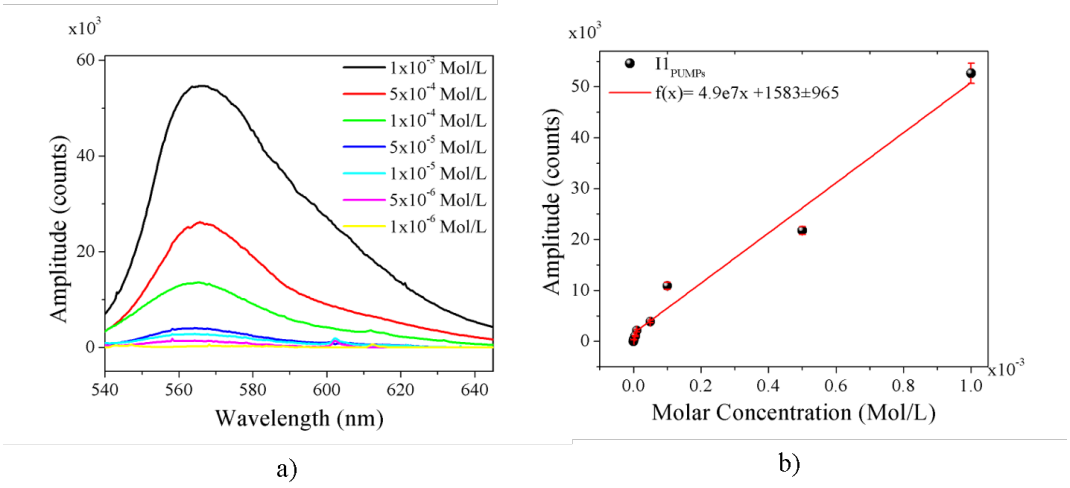

FIGURE 3.5: Fluorescence spectra acquired from the complete set of aliquots taken at I1. **a)** emission spectra for the different molar concentration, **b)** the maximum amplitude value from each spectra on **a)**, in addition the best fit of a linear approximation is shown.

A set of 20 acquisition spectra was acquired for statistical purposes. Between the different molar concentrations, the device was cleaned by allowing the solvent (buffer) to recirculate for 20 minutes. After this, the next measurement was focused first on ensuring the same level of noise. Once the parameters are restored, the next concentration is pumped and the acquisition follows as the discussed protocol.

The Figure 3.5 a) shows the characteristic emission spectra of the RB at different molar concentrations, acquired both at the inlet I1 and under the protocol presented above.

From Figure 3.5 (b) the best fit presents the dependence of the molar concentration with the amplitude and this is finally used as a guide to experimentally determine the corresponding molar concentration along the device (from P1 to P3). The curve presents a linear behavior as expected (Fang et al., 2011; Chabinyc et al., 2001)). Briefly, from the equation describing the trend, x is the molar concentration while f(x) the associated intensity and in this way, whatever the fluorescence amplitude, this corresponds, through the adjustment equation, to a given molar concentration along the microdevice.

Once calibration curve is done, we are able to carry out fluorescent emissions as an indicator of fluorophore molar concentration along the three designated points, P1, P2 and P3, Figure 3.6 a) represents how the intensity, in logarithmic scale and with the corresponding statistical error, evolves along the three selected points while, Figure 3.6 b) and c) show two examples of how molar concentrations evolves along

the points under two initial concentrations $1x10^{-3}$ and $5x10^{-6}$ Mol/L. The experimental measurement of molar concentration threshold $0.5x10^{-6}$ Mol/L was obtained and registered respectively by pumping the system with 5 $x10^{-6}Mol/L$ and measured at the P3 point. By pumping with 1 $x10^{-6}Mol/L$, the experimental data obtained at P1 was proportional to the noise level of the system in counts.

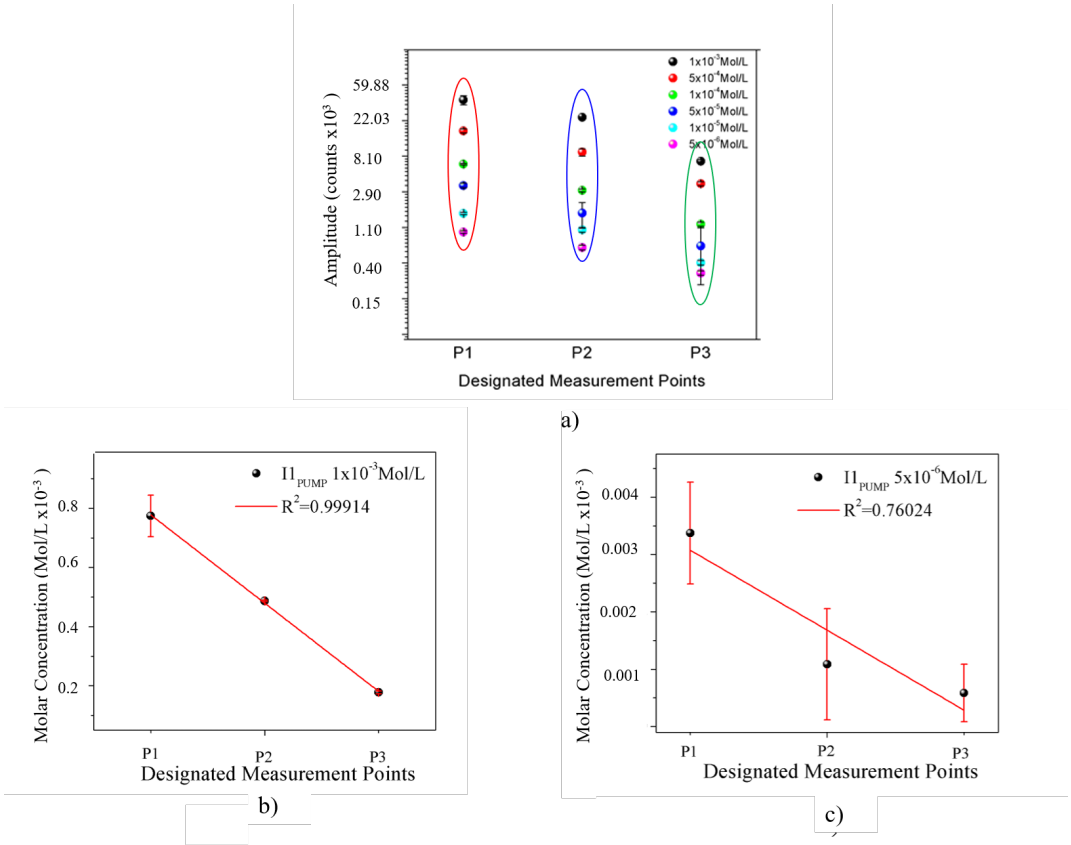

FIGURE 3.6: Maximum fluorescence spectra amplitude acquired in P1, P2 and P3 from **a)**: ehe collection from the entire set of aliquots (Ln scale), **b)** : $1x10^{-3}$ Mol/L and c) : $1x10^{-3}$ Mol/L.

Forming the set of points presented in Figure 3.6 b) and c) by considering the fitted equation for calibration, it is possible to associated finally the corresponding molar concentration from the set of fluorescence amplitudes, Figure 3.7 a).

From Figure3.6 it can be observed that the experimental accuracy decrease, because the error enhances as the molar concentration also decreases.

After carrying out all the measurements of the aliquots, these were compared with those obtained from simulations. The Y-serpentine shaped geometry was recreated, with exactly the same geometric characteristics of the microchannel, in addition a blank material was simulated using the main properties of the Rhodamine B dissolved in methanol, following this consideration, and taking into consideration the **laminar flow** and the **transport of diluted species** from the COMSOL physics module, the mixing process between different molar concentration (RB and methanol) were carried out. The evolved concentrations in simulation were taken into at the selected region defined in experiments (P1, P2 and P3) (see Figure 3.6 a). These values are compared with those from experiments, Figure 3.7 b).

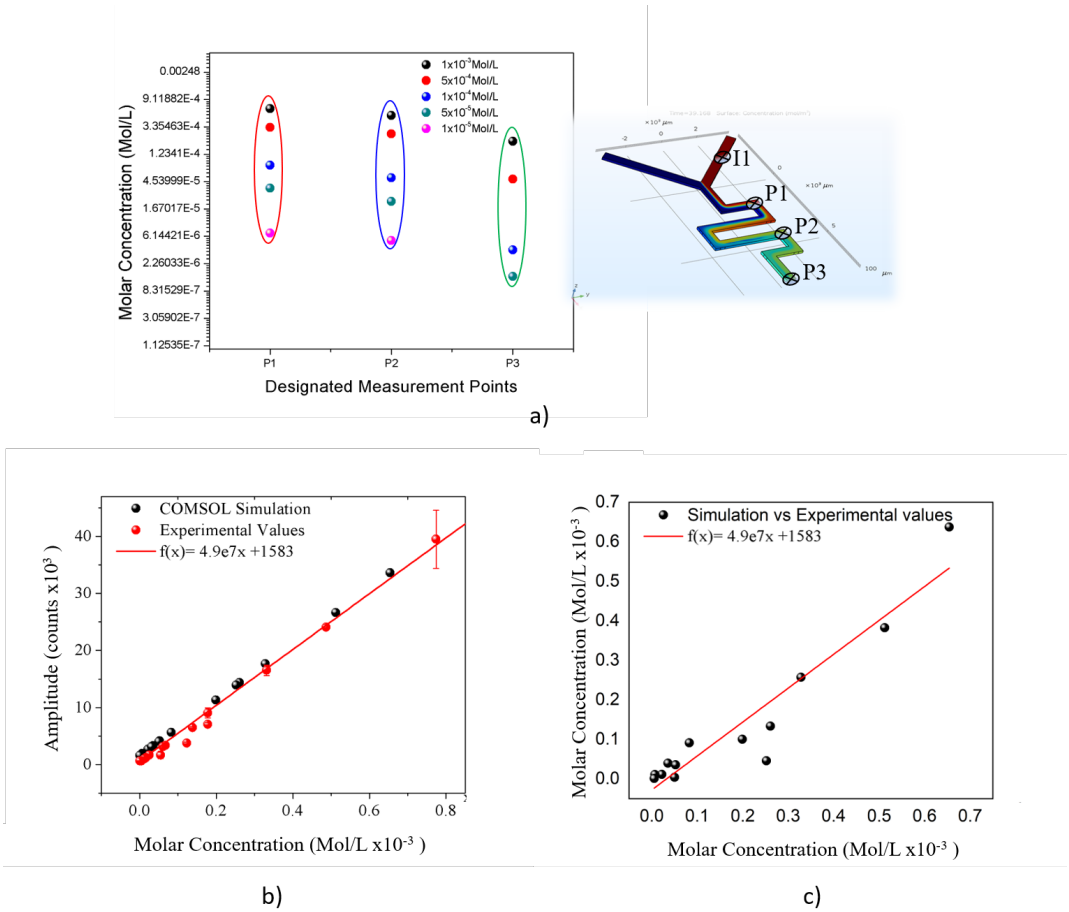

FIGURE 3.7: **a)** The simulated values of molar concentration in each of the designated points over the Yserpentine-shaped geometry, showed at the right of the graphic, **b)** concentration values acquired in the experimentation compared with the simulation values from COMSOL, in addition, the calibration curve is added, **c)** values from COMSOL simulation in function of the experimental data, in addition the calibration curve is plotted.

Figure 3.7 b) shows how the acquired experimental values and data from simulations strongly coincide in trend and magnitudes which highlight the reliability of both experiments and simulations. Figure3.7 c) presents how concentrations from experiments and simulations relates; red line, the best fit from experimental points, showing a percentage of variation (R^2) of 0.85 demonstrating that the variation of the results can be explained from the uncertainty in the concentration values of each studied aliquots to the experimental performance.

Chapter 4

Microparticles sorters: Perspectives

Sorting, detection and separation of micron size particle have been received an enormous attention in the scientific community, for example, the impact in the society are mainly focused on illness diagnostics, chemical species separation and drug delivery. In microfluidic there exist two types of particle sorting systems: the active and passive method. Active methods such as that based on fluorescent labels, another that implemented magnetic fields (magnetophoresis) and also others where the system is based on acoustic interactions (Shields IV, Reyes, and López, 2015; Kirby et al., 2012; Shi et al., 2009), are few examples well established in the state of art to manipulate and separate cancer cells for biological purposes. The fabrication and application of active method, in terms of lab-on-a-chips (LOCs), represent a high cost because of the laboratory requirements. Moreover, the additional transducer components from the LOC, applied to manipulated particles causes the cost to rise in terms of more fabrication procedures and more sophisticated laboratory equipment. In this way, these active platforms are out of the focus of this perspective work. In the other hand, passive methods offers separation of particles at the microscale taking advantage of their sizes (Zhang et al., 2006), flow focusing (Lei et al., 2020), traps (Lee, Mena, and Burns, 2019) and inertial flow method (Kuntaegowdanahalli et al., 2009) are few of the methods that take advantage of the microchannel geometry for the separation of particles. These systems have the capability to separate particles or cells with geometrical properties ranging from 10 μm to 20 μm o diameters and, can be applied as microparticle sorters with optical and/or mechanical transducers for detecting and visualizing particles in real time, represent a punctual opportunity to early detect illnesses and moreover, to early develop medical diagnostic. In Figure 4.1, presents the most recent methods to sorting particles through microfluidic systems.

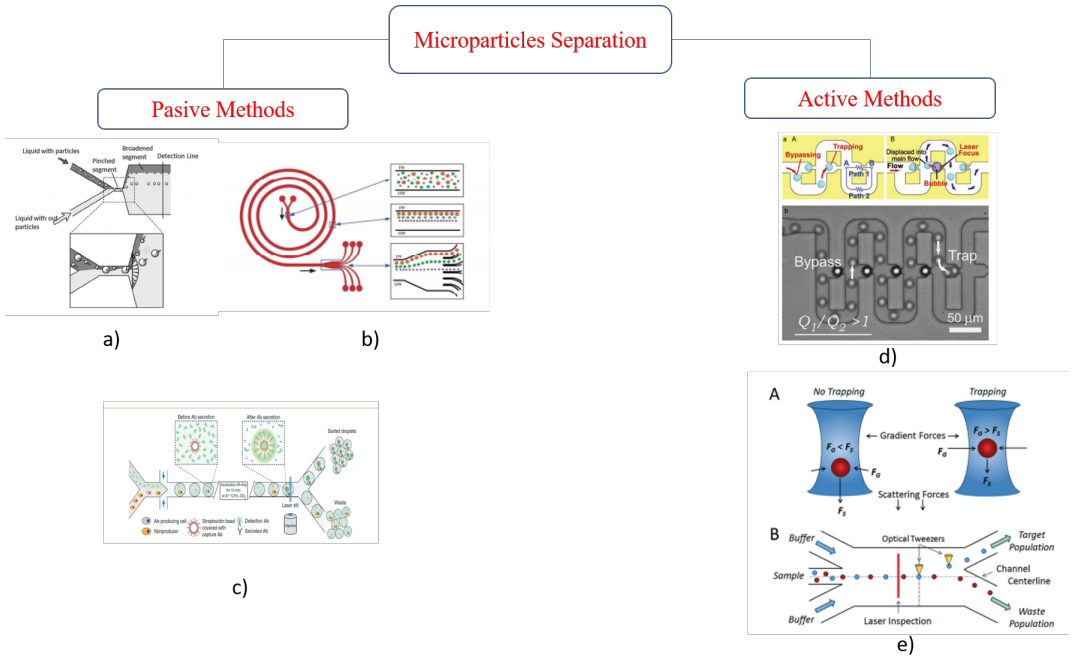

FIGURE 4.1: State of the art for microparticles sorters and selectors devices in a) an hydrodynamic separation, b) inertial force), micro-droplets isolation, d) a size trapping selection and e) optical tweezers selection.

4.1 Overview of microfluidic particle sorting designs: a fabricated punctual example

One of the most frequent problems in filtering particles is the particle clogging effect. To avoid this problem and by considering the passive method, many strategies can be developed to increase the filtering efficiency by developing clogging-free microchannels. For example, the continuous crossflow and inertial focusing technique have been widely employed in free-clogging microchannels.
Different parameters in the microchannel geometries are modified with the aim to separate microparticles such as: straight channels with expansion-reduction size. In this work, the fabrication of many expansion-contraction channels along the microfluidic system were considered to avoid the clogging effect as a first approximation to manufacture and characterize microfluidic systems based on passive methods with good opportunities to manipulate and separate particle at micrometer scales which, represents another proposed objective of this work. Although different designs of microparticle sorters were studied, we report only one fabricated model.

The global fabrication protocol was based on direct laser writing as exposed above and simulations were carried out through COMSOL-Multiphysics.

Once the new master mask is developed, the geometrical details were recorded to replicated in simulations. In addition, the experimental fluid flow properties, in the straight expansion-reduction microfluidic system, was also replicated. Figure 4.2 shows the most representative simulation which range from flow velocity to streamlines. Figure 4.2 a) and Figure 4.2 c) are those for flow velocity. These simulations show the variation on the flow velocity when this goes inside the slits zones in the micro-device. The scale bar in *m/s* shows that those regions of red color are the regions with the highest velocity while those in blue are the lowest one. In this

sense, simulations show that once the fluid goes inside to the slits area, the flow rate increase twice ensuring that the pressure in and pressure out keep constant. In addition, Figure 4.2 b) shows the generated vortexes in the slit regions which helps the system to avoid the clogging effect discussed above. It can be observed that due to the cross-flow produced by the interaction between flows from I2 and I3, a vortex appear near to the slits. Finally Figure 4.2 c) shows the two spliced simulations (flow rate and streamlines) and, it is possible to observe that for those regions with concentrated stream lines, the flow rate is higher.

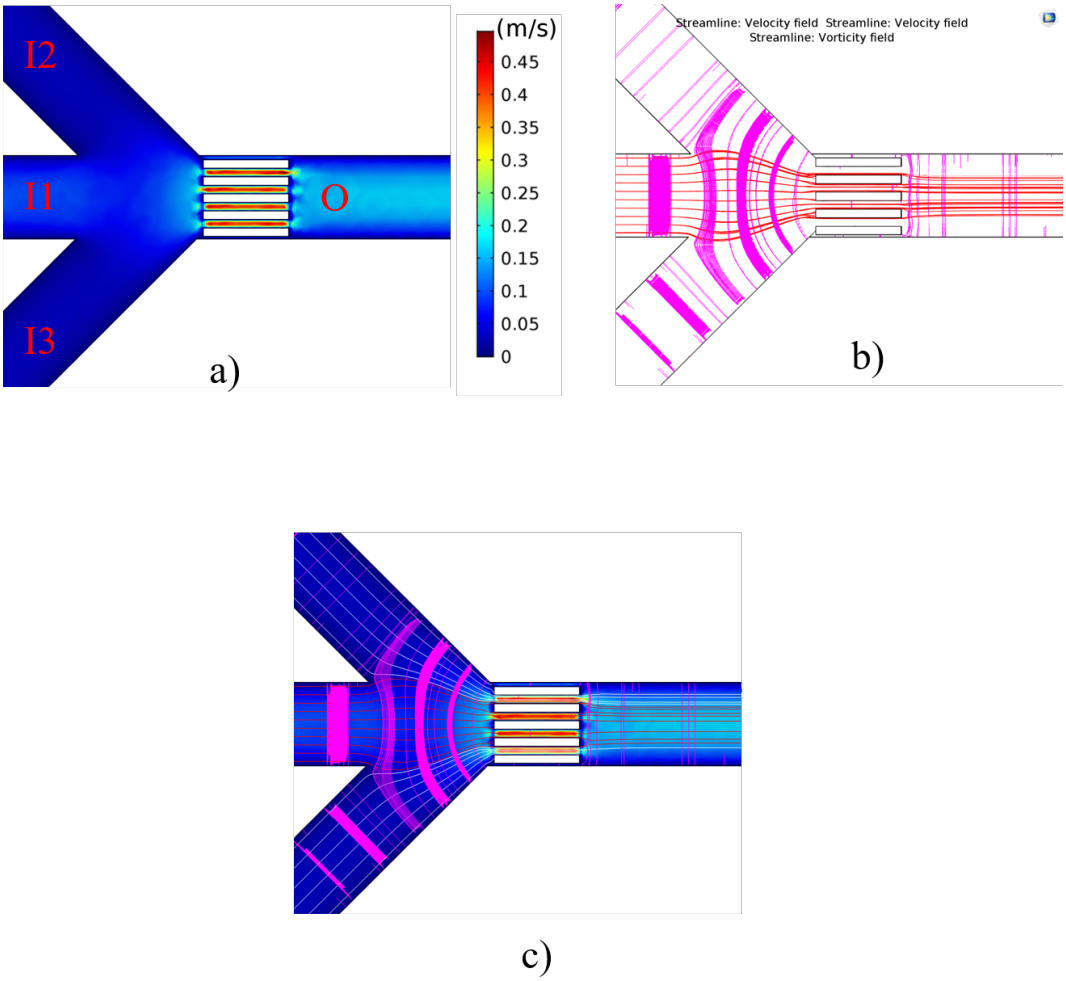

FIGURE 4.2: a) Velocity magnitude of the fluid in the microchannel, b) streamlines of the fluid and c) velocity magnitude plus the streamlines, in magenta the vortex generated by the cross flux coming from I2 and I3.

The design of straight channels with expansion-reduction size highlight the opportunity of filtering particles suspended in a poly-dispersed solution. Moreover, these systems avoid the clogging effect because of the vortex produced along the cross-flow generated by three different inlets. Even the fluid flow in the microchannel is under the laminar regime, Re < 20, it can be observed the formation of vortex produced by the cross-flow between I1, I2 and I3. The flow rates, density and dynamic viscosity used in the simulation are presented in the Table 4.1

	$\rho(Kg/m^3)$	Flow rate I1 (ml/min)	I2 and I3 (ml/min)	μ (Pa*s)
Blank material	1000	0.5	0.3	0.001

TABLE 4.1: Parameters used in the COMSOL simulation. As it can be observed, the properties are the same as the water.

4.2 Proof of concepts

Once the device was fabricated, the new microfluidic platform was used to transport PMMA particles with 10 μm of diameter. Briefly, the device was fabricated under the same laser-writing protocols while the particle tracking was carried out through video microscopy studies. The microfluidic chip rested on a 3D-printed holder which was designed to hold the device and prevent mechanical movement due to the micro-tubing. As presented in the Figure 4.2 a) the device contains three in-ports, I1, I2 and I3, from where the particles flow inside the micro-chip. Respectively, I1= *0.5 mL/min* and I2=I3= *0.3 mL/min* were the used flow rates. Figure 4.3 shows the image of the experiment where the device is tested for fluid leakage.

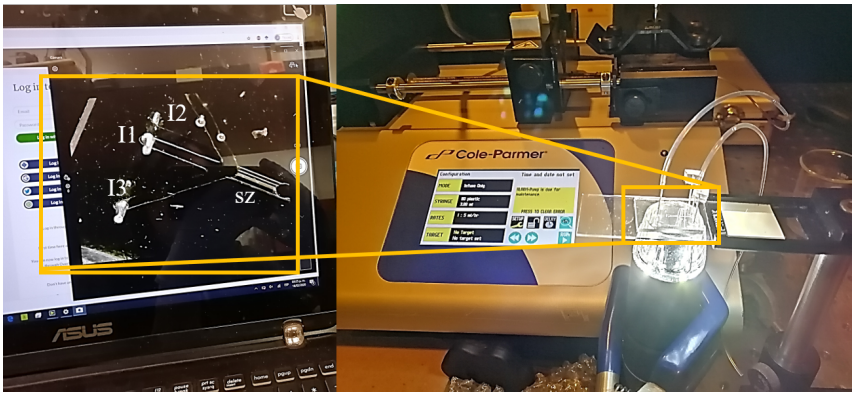

FIGURE 4.3: Experimental test of fluid leakage. It is possible observe a microcamera, the employed micropump, serynger and the system to visualize the device. in the inset are shown the sorting zone (SZ) inlets I1, I2 and I3.

Figure 4.3 shows the microfluidic device from which it is noticeable that the device has good contours and its printed arms have good quality. The used protocol to monitor the tracking of particle was video-microscopy (Trivedi et al., 2015; Di Leonardo et al., 2006; MacDonald, Spalding, and Dholakia, 2003). Video-microscopy is a well accepted techniques that allows the analysis of the fluids and contents at different flow rate. The experiments, as visualized in Figure 4.3 contains a CCD-camera which is placed below the microfluidic device to track the particle paths once these flow along the microchannel configurations.

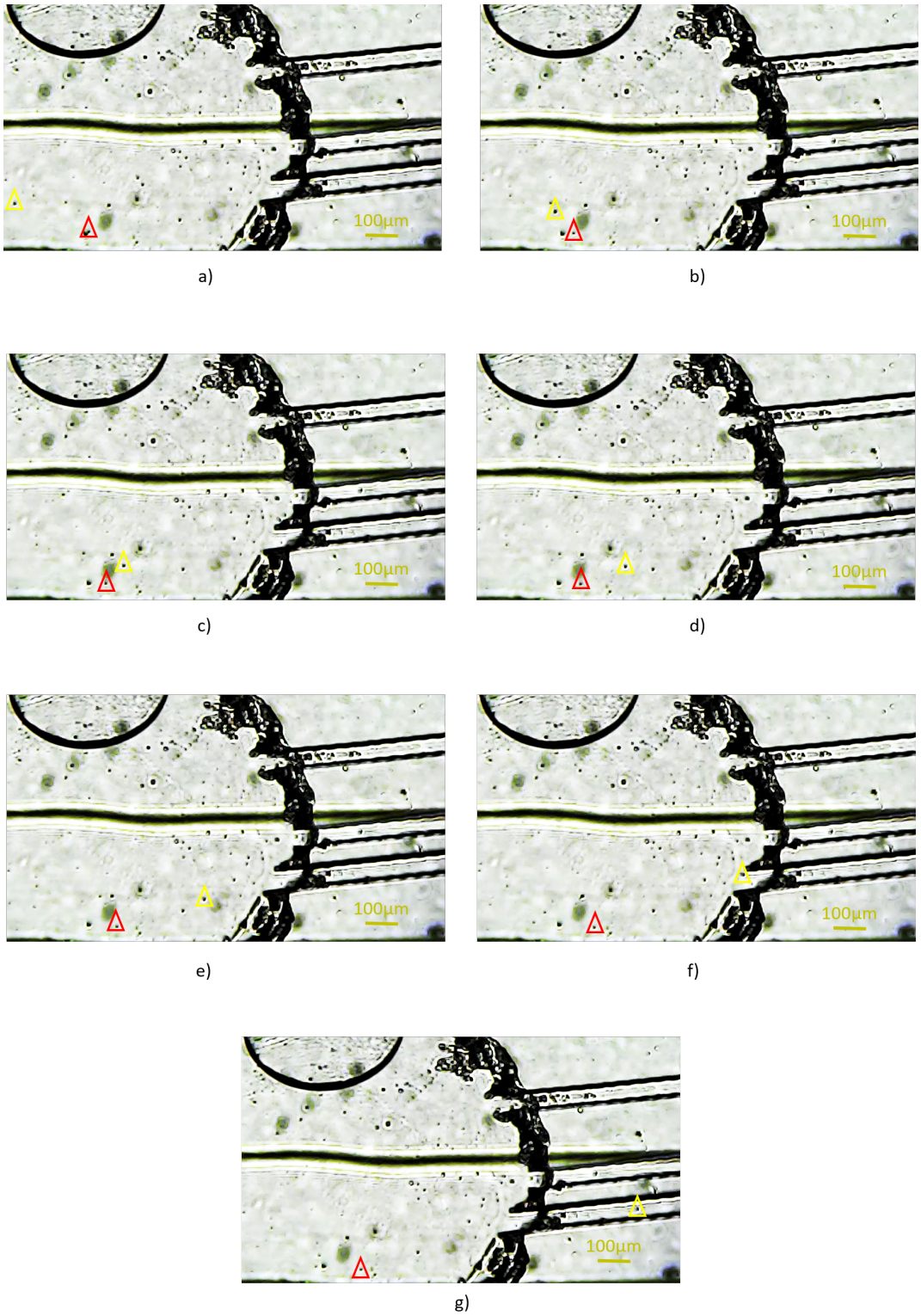

FIGURE 4.4: Tracking the position of two particles remarked into the red and yellow triangles. The frames evolution goes from a) to g)

From Figure 4.4 the black line is a deffect of the SLG substrate, in addition, it can be observed a half circle that connect the big channel with the sorting zone, this is because the focused laser beam has this form and is not a rectangle polymerization process. Figure 4.4 shows a set of pictures where the particle tracking is observed for different positions inside the channels. The positions are purposely highlighted

for the 10 μm PMMA particles. As can be observed , the velocity of the particles depends in the relative position of the particle by following the triangles it can be observed that the yellow triangle has a position near to the center of the channel meanwhile the red triangle has a position far away from the center, this produce that the magnitude of velocity of the particle enclosed by the yellow triangle is bigger than the red triangle, this observation match correctly with the COMSOL simulation showed in Figure 4.2.

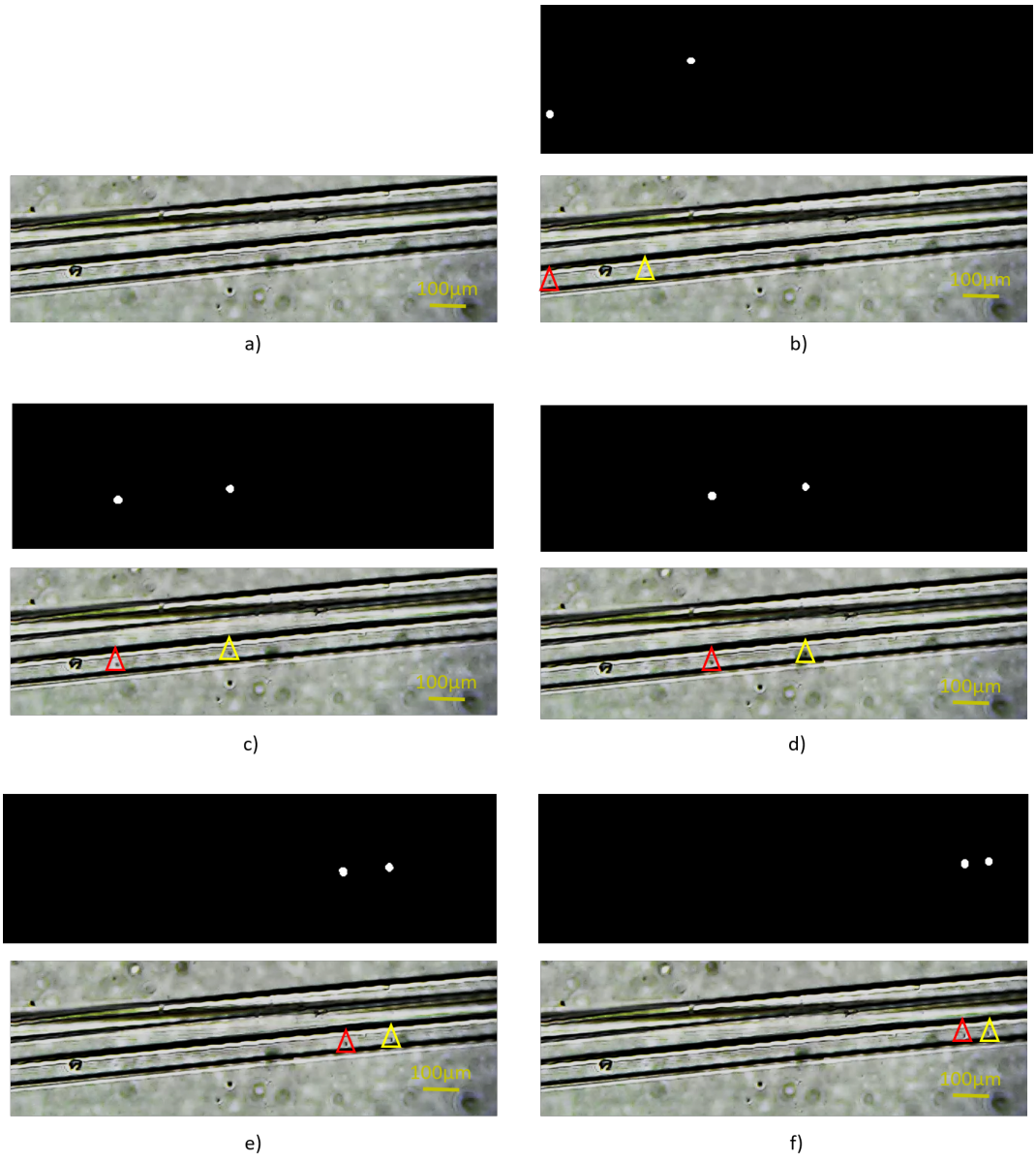

FIGURE 4.5: Particle tracking within the slits in the sorter microsystem. The frames evolution goes from a) to f)

In Figure 4.5 it can be observed a similar situation as the Figure 4.4 but the change in the magnitude of velocity between the tracking particles is lower than the first case. In Figure 4.5 the relative position of the particles is not so different within the slits, so is observed that the particle enclosed in the red triangle almost reach the position of the particle enclosed in the yellow triangle due to the different velocity acquired by each particle position. Different from Figure 4.4, each image in Figure

4.5 contains a post digital image processing to track the particles of interest, to do that, an algorithm to obtain the average was employed to clean the image, this allows us to track the position of the particles. The observed results, in the magnitude velocity of fluids matches with the COMSOL simulation.
It is necessary mention that the simulation results were compared with the experiment only for the velocity magnitude, in addition, the images were acquired by a nonprofessional microcamera, thus, the acquisition of images from a video have not a highly precision. Nevertheless, the images are very useful to observe the particle behavior into the microchannel.

Chapter 5

Conclusions

Through this thesis work, multiple optical, chemical and electronic techniques have been employed to fabricate and characterize microfluidic devices that range from micromixers to microparticle sorter. First, the 3D mechatronic system and the physical description about how focused light interacts with SU8 photoresist, is presented. Then, the detailed overview of the master masks fabrication for micromixers and particle sorter designs is presented, as well as the device qualities from master mask to chips-presentation. The laser printing technique it is now considered in our laboratories such as potential tool to fabricate simple and complex master mask-circuitry. Micromixers and finally, particle sorter, were the fabricated microfluidic chips studied in this work. The micromixer based on Y-serpentine shape allowed measuring, in real time, the changes of molar concentration of chemical fluorescent solutions. The chip based on microfluidic mixer used the fluorescent technique to constantly monitor the fluorescent emission amplitudes from different aliquots along the microchanels. The full characterization protocol is presented in detail in chapter 3. In addition, the results were compared with those obtained from simulation based on finite element method. **Laminar Flow** and **Transport of Chemical Species** were the implemented studies in COMSOL Multiphysics to carried out the simulations based on molar concentration evolution. Both, experimental results and simulation were finally compared demonstrating the high accuracy of the platform to reproduce those results obtained in simulations. In addition, a particle sorter was developed and applied. From master mask presentation, the device presented some size limitations because, the maximum printed size of its channels was $50\ \mu$m limiting the sorter condition at this size. Nevertheless, it was possible to track the position within the sorter region of 2 PMMA microparticles by applying simple microcamera and digital image processing, this, allows us to compare the COMSOL simulation results for the velocity magnitude and the experimental observation, qualitatively. In this way, the microfluidic chips presented in this work establish the initial conditions for more potential applications related with chemical species mixing for micromixers and selection of interested particles in circulation for particle sorting.

Appendix A

.1 Fabrication and programming of a 3D platform

The fabrication of a 3D platform (3DP) had the goal to achieve mechanical resolution of 3 μm of minimal advance. For this, the employment of Nema 17 stepper motors (SM), Easy drivers V4.4 , spindles and its mechanical and electronic details were taken into consideration for the mechanical design, in addition, a home-produced software is presented and discussed in this section.

.2 3D Platform Design

Platform size, weight optimization, high mechanical resolution and simultaneously three axes control were the main objectives in the platform. To reach this, each mechanical element which constitute the 3DP were manufactured by a 3D printed process, or acquired in aluminum pieces for the manufacturing process. For the printing manufacturing pieces, they were designed by SolidWorks software, in this, the well functionality and assembles were investigated. The mechanical designed details an artistic render representation is showed in Figure 1.

These items constitute each linear platform and form the conversion mechanism from circular movement to linear motion, achieving the transmission through the nut holder. Because one of the discussed goals on this platform was the weight, different pieces of the 3DP were 3D printed by using PLA material which offers resistance and durability. Moreover, tbecause the weight of the entire system was reduced, it allowed us to avoid the backlash caused by this.

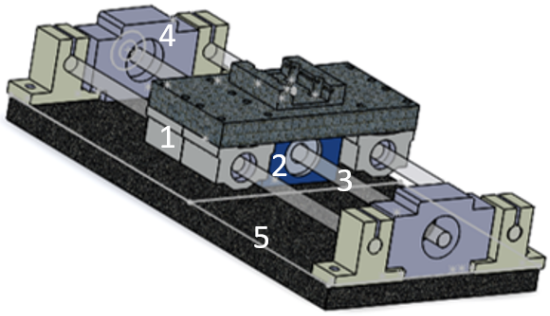

FIGURE 1: The items used to arm a linear platform are presented. 1: the linear rolls, 2: the nut holder, 3: splindes free roll er, 4: coupling system between the holder-free roller and 5: the assembled set of pieces.

The size dimensions of the 3DP were performed according to the sizes of the polymeric micro-structures to be fabricated (microfluidic masks). The 3DP is constituted by three individual linear platforms as the presented in Figure 1, each platform was assembled by using the follow mechanisms presented in Table 2:

Mechanical Device	Employed
Spindle	1
Stepper Motors	1
Couples	1
Linear Bearings	2
Steel Bars	2
Bars Holder	4
Bearing Holders	2
Spindle Nuts	2
Nut Holder	2

TABLE 1: Employed devices to fabricate each of the three linear platforms.

By combining translations mechanisms, free roller with a rotational ratio of 2 $\frac{mm}{rev}$ (APR) and the electronic systems as driver-SM with 200, 400, 800, 1600 and 3200 $\frac{step}{rev}$ modes (SPR) it was possible to reach a high mechanical resolution (MR). The equation that describes the theoretical MR achieved by involving the APR and SPR is presented in Equation 1 here, the conversion of rotational to linear motion is implied.

$$MR = \frac{APR}{SPR} \tag{1}$$

Given this, the mode of 1600 $\frac{step}{rev}$ was chosen in the driver, allows us to access to mechanical resolution of 1.25 μm of advance per step in each stepper motor (SM). Figure 2 shows an image of the newly built 3DP, already present in the Biophotoacustic laboratory at the DCI.

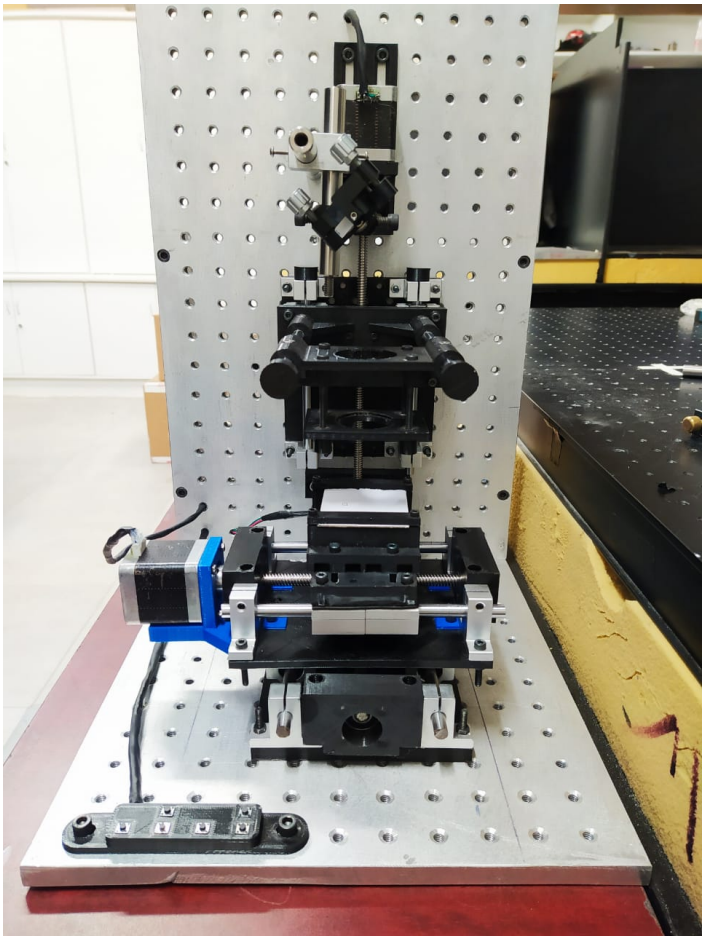

FIGURE 2: Fabricated 3DP. It is observed two linear platform one on top of another and another platform in the top, in addition, the image shows the PLA polymer printed and the aluminum pieces.

With the 3DP totally manufactured, the testing of the system in terms of resolution and functionality were carried out by programming the theoretical displacement of the platform. By measuring the experimental displacement in repeated times. These data were considering in the fabrication protocol to ensure the well-polymerization of the SU-8.
The results of the measured displacement and its variations are shown in the next subsection.

Experimental measurements of resolutions

By using the LabVIEW-Arduino interface (LAI) and the EasyDriverV4.4 (ED) and once the 3DP was fabricated, multiple displacement measurements were carried out to mechanically characterize this. The linear platform located at the bottom of the used 3DP system was employed for this initial mechanical characterization because the this support more weight.

These measurements resulted in an improvement of 95% respect the mechanical resolution available in our group with the other platform. Table 2 shows the recovered data from these experimental measurements.

Measure	Experimental Distance (μm)	Experimental Distance (μm)
1	30500±356	10200±227
2	30300±356	10100±227
3	29800±356	10000±227
4	30100±356	210300±227
5	30500±356	10400±227
6	30400±356	9800±227
7	30200±356	10000±227
8	29800±356	9700±227
9	30000±356	10000±227
10	29400±356	10200±227

TABLE 2: Experimental measurements carried out in the linear platform, the correspondent standard deviation is plotted in Figure 3.

The experimental measurements were carried out at two different set of parameters (doses): 2800 and 400 $\mu m/$s for 30000 and 10000 μm respectively. Nevertheless, this variation represented only the 1.2% for the lowest velocity and 2.27% respect the desired displacement. From this and given the microfluidic application it was decided to use a velocity of 400 $\mu m/$s for the master masks (MM) fabrication. This velocity, in addition, is the optimum one according to the size of the achieved polymeric micro-structures. Moreover, fabrication testing showed that the selected doses allowed us better quality on the SU8-polymerization than the fastest one. For the test, it was chosen the larger displacement due that the error is accumulative and its influences can be best appreciated in this way. The variation in each measurement was directly associated with the mechanical backlash, which was inherent in the mechanical system and depends in different factors such as the weight and mechanical components quality, this backlash could be reduced by the implementation of lock-nuts, which ensures the position of the sample along the motion in the experimentation and by reducing the total weight to be moved.
Plots of the experimental measurements of distances are presented in Figure 3.

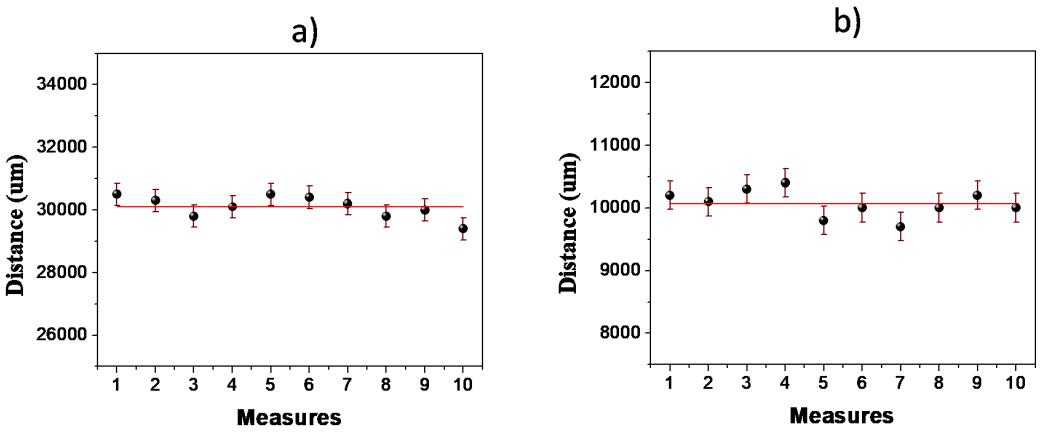

FIGURE 3: Plots with the measured displacement in one of the three linear platforms. a) shows the data corresponding to 30000μm and b), 10000μm. Each of measurement was taken with a velocity of 2800 and 400 $\mu m/s$ respectively.

From Figure3 it can be observed that the experimental data from both distances oscillates around the central value. For the 30000 μm the standard deviation obtained was about 356μmm, while for the 10000 μm, the standard deviation was 227μm. The obtained results gave us a high certainty with respect to the required precision for the MM fabrication.

The used mechanical equipment to measure the displacement of the new 3DP under discussion was the Vernier. The instrument presents itself a mechanical error of 20 μm.

LabVIEW Programming

In order to fabricate the desired geometries of $\mu - fluidics$ master masks, a home-produced LabVIEW programming environment was developed. For this, the LabVIEW-Arduino Interface (LAI) was widely employed which allows us simultaneously control the three linear platforms which offers an extraordinary opportunity to develop complex geometries.

The 3DP is entirely controlled by the home-produced LabVIEW code, the block diagram of the different SMs control follows the steps illustrated in 4 and enable the communication between computer and the mechanical system through the electronics components. The LAI was employed to communicate the Arduino with each SM driver which send a pulse width modulation (PWM) electrical signal to execute the micro-steps. The evaluation of the related work focuses on three issues: developing a graphical interface for the 3DP control based in LabVIEW, the fabrication of MMs and the fabrication and operability of the final microfluidic chips.

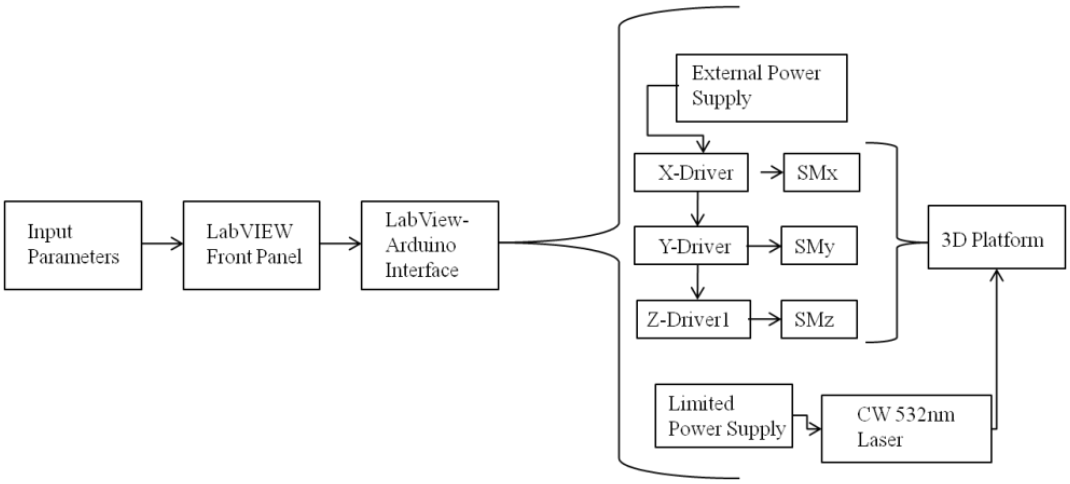

FIGURE 4: Schematic System to fabricate the microfluidic master masks.

The very first instruction to create the communication in the graphical interface is initializing LAI. To carry out this it is necessary to introduce some input parameters showed in Figure 4. Many event structures (ES) were created into the Block Diagram to select the "action" to be performed. Each ES contains the instruction for the Driver-SMs and for each master mask pattern, there exist a corresponding ES. The ES are finally activated by different buttons placed in the Tab Control (interface) contained in the Front Panel.

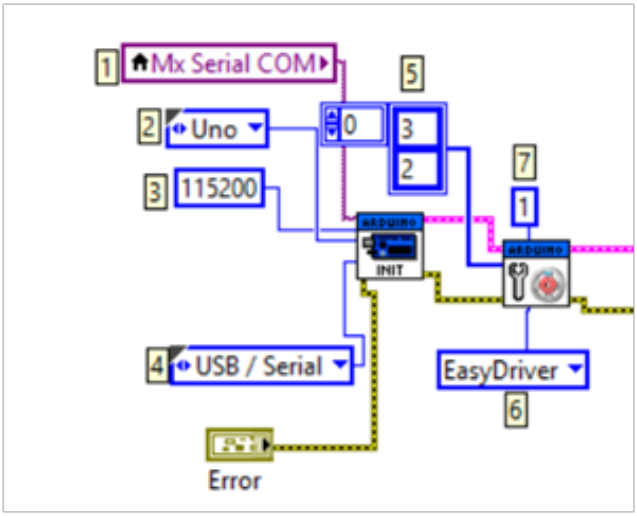

FIGURE 5: LAI initialization and configuration. 1: channel number of serial communication with the Arduino, 2: Arduino Board Type used to control the SMs, 3: specified Baud Rate, 4: Connection Type, 5: Stepper Pins to communicate with the 6: the EasyDriverV4.4 control Method and finally the Stepper to select stepper and direction.

Parameters such as velocity, numbers of steps (displacement length in the platform), direction and synchronization between each instruction are the base to the correct printing of patterns. Externally, the code block receives that information (from the user), particularly, the length in x, the direction in y (Lx and Ly), the velocity in x (Vx). By introducing these parameters in the vectorially form, it is possible

to draw curves with an specific angle between each others and by combining these, to produce microstructures applicable in microfluidic patterns.

The parallelism of the process is accomplished by LabVIEW environment, here, by using the *While structure* and the ES, it is possible to select which geometry pattern will be produced. In order to create inclined lines, it is necessary the parallel movement of both SMs, for this, some parameters mentioned above for SMy were established such as function of the input parameters to SMx in the Front Panel, as in shown in Figure 6.

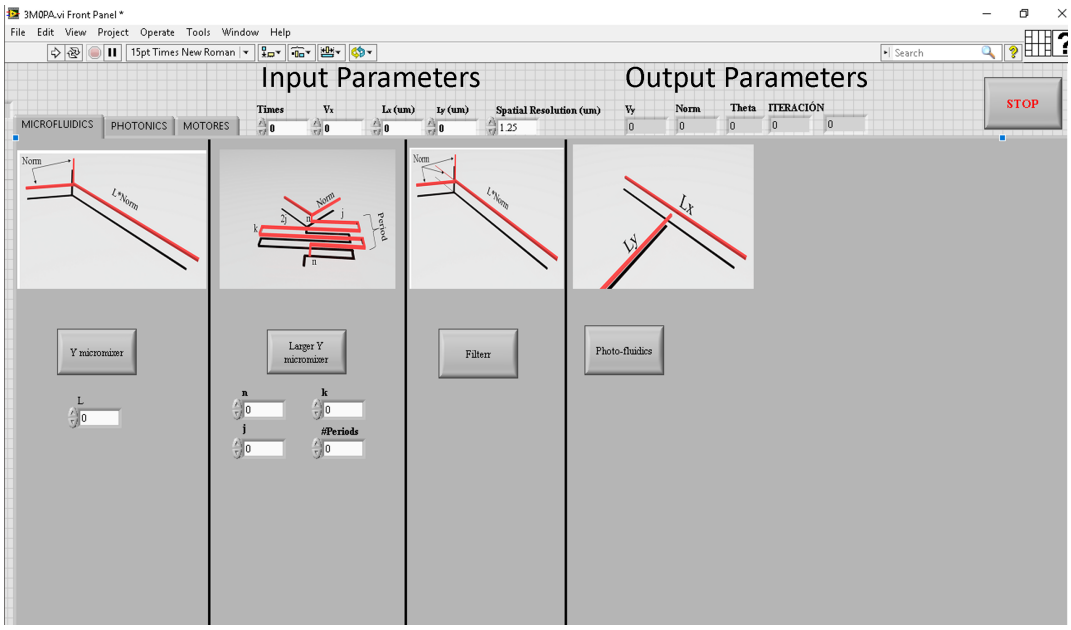

FIGURE 6: Front Panel: In this interface, the user can introduce the selected parameters to fabricate the MM.

Vx is introduced externally and the velocity in the y direction (Vy) is constrained and obtained by the relation $Vy = \frac{Vx*Lx}{Ly}$ which ensures the parallel movement between SMs once the Lx and Ly are given. In addition, the distance in sloping lines is $Norm = \sqrt{Lx^2 + Ly^2}$. with an angle $\theta = \arctan(\frac{Ly}{Lx})$.

All of this is calculated simultaneously and the process is carried out in the time out for ES and it is shown in theFigure 6.

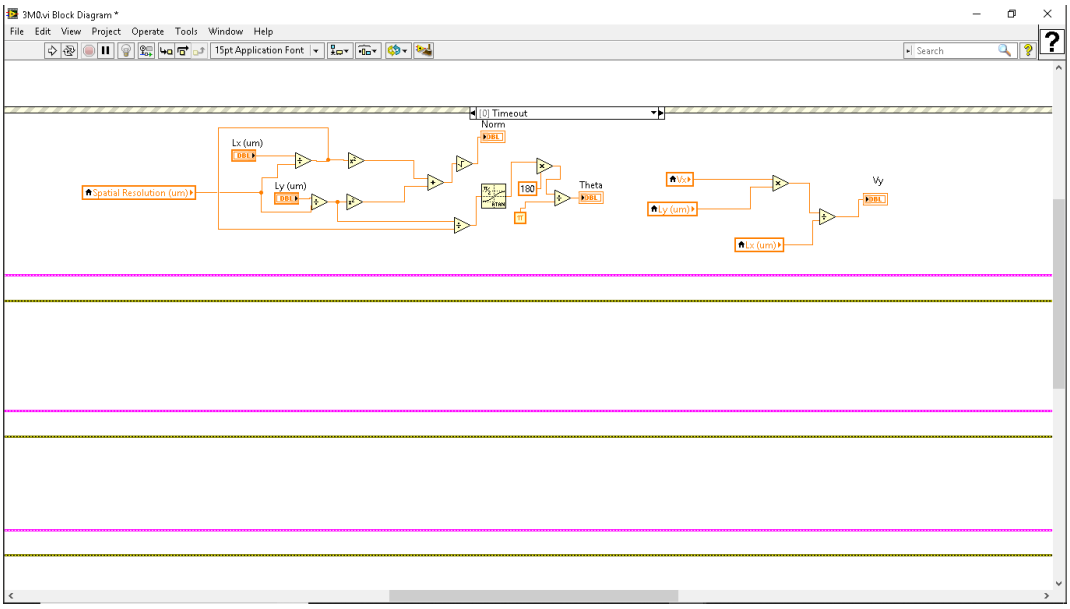

FIGURE 7: ES for time out: In this ES the output parameters are calculated. All of them are shows in the front panel.

Finally, the communication LAI-3D platform is achieved by electronical and mechanical devices. The information contained in the interface is sent to each Easy-Driver through the Arduino and, in turn, this is decoded into electrical pulses in the SMs. The mechanical components and the drivers microstep selected allowed us tmechanical resolution of 1.25μm. Although this exceeds what is needed (for microfluidic purpose), it gave us a good control on the shapes, which is proportional to the high quality aspect ratio in the master mask fabrication. Figure 8 shows an example of the programming for the simplest Y-shaped MM.

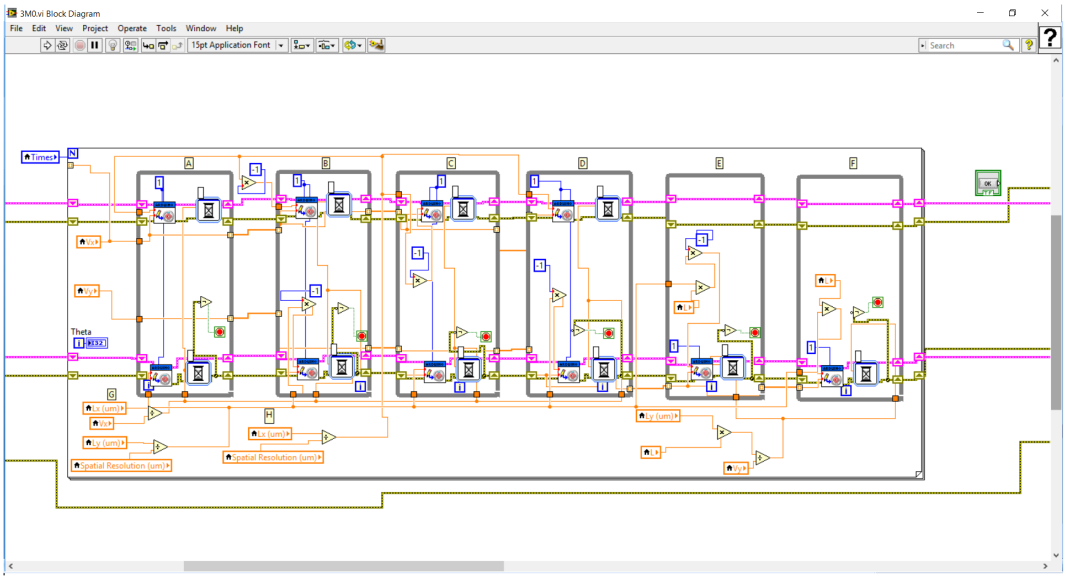

FIGURE 8: Block Diagram for the Y-shaped master mask fabrication. **A, B, C and D:** Paralleling movements of SMs, this create the I1 and I2 arms forming an angle of 45° with the mixing channel.**E and F**: form the mixing channel.

By following the presented protocol in Table 2in chapter 2, a Y serpinte-shape

MM was fabricated. The parameters are introduced in the Front Panel and processed in the block diagram to produce the movement of the 3DP.

Appendix B

.3 Results

Rhodamine B, the used commercial dye, is a fluorescence compound with a very strong optical absorption at 549 nm and with principal emission centred at 564 nm. Respectively with line widths of 130 nm and 190nm respectively and a Stokes shift of 20 nm, Figure 9 shows both: the aliquots and the light emission and absorption spectra of R6B.

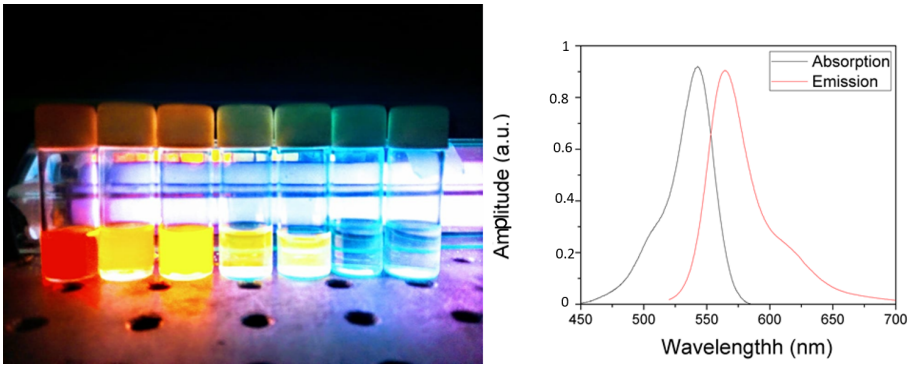

FIGURE 9: Optical absorption and fluorescence emission spectra from an RB aliquot at $1x10^{-3} Mol/L$.

The emission and absorption properties allowed us to implement a method to measure the evolution in molar concentration along the microfluidic channels by fluorescence spectroscopy protocols. By preparing a set of solution's of RB in methanol (aliquots), each corresponding injected molar concentration inside the chip could be associated with a fluorescence intensity and, in this way, a linear regression is obtained where the fluorescence intensity and concentrations were finally related through an equation.

Once each aliquot and mixture is injected inside the chip, these were optically pumped by a CW 532nm laser. The fluorescence emission spectra were acquired along designated points at the microchannel where, an OCEAN OPTICS spectrometer 3000 series were employed to recorded the emissions in the range of 300-850 nm. 500 ms of integration time and an average of 20 measurements (for statistical purposes) were the experimental parameters for each measurement. Aliquots volumenes of 500 μliters o were used to acquired the fluorescence amplitudes to be associated with the corresponding molar concentration from the discussed equation.

Complementary micromixer calibration

Figure 10 shows the complementary calibration points experimentally acquired, in addition to the results shown in chapter 3 .

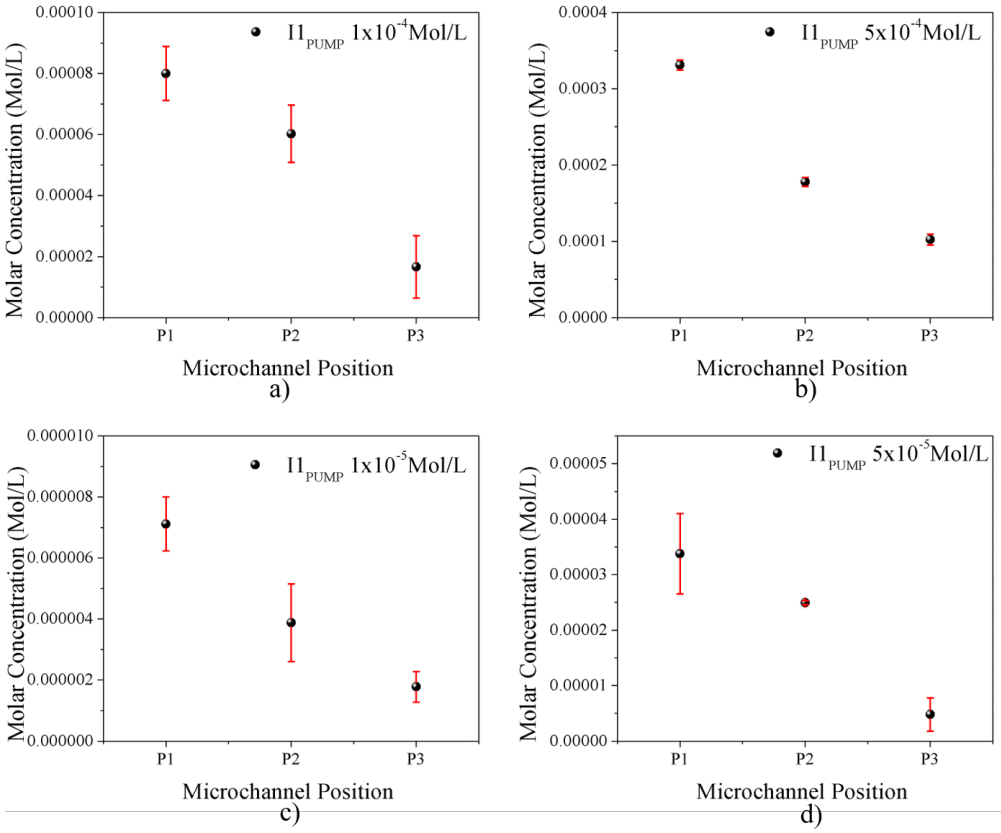

FIGURE 10: The evolution of molar concentration measured in the three fixed points of evaluation for **a)**: $5x10^{-4}$ Mol/L, **b)**: $1x10^{-4}$ Mol/L Mol/L,**c)**: $5x10^{-5}$ Mol/L and **d)**: $1x10^{-5}$ Mol/L.

It can be observed that the evolution of the molar concentration along the microchannel has the same tendency as presented in chapter 3. For the lowest molar concentration, the tendency is lost because that range is close to the minimal resolution. In addition, it is shown that, the accuracy in the measurements decreases when the concentration does.

CONACYT | CENTRO DE INVESTIGACIONES EN OPTICA, A.C.

León, Gto. 27 de julio de 2020

Dr. David Delepine
Director de la División de Ciencias e Ingenierías
Universidad de Guanajuato, Campus León
PRESENTE

Por este conducto manifiesto que he leído la tesis "Design, fabrication and implementation of microfluidics systems applied in chemical micromixers and particle sorters" que sustenta el C. Jonathan Ulises Álvarez Martínez (NUA 426639), bajo la asesoría del Dr. Rigoberto Castro Beltrán para obtener el grado de Maestría en Ciencias Aplicadas; así mismo avalo el contenido del documento como un trabajo de tesis de maestría.

Sin más por el momento, le envío un cordial saludo.

Atentamente,

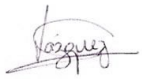

Dra. Gloria Verónica Vázquez García
Investigadora titular
Centro de Investigaciones en Óptica

UNIVERSIDAD DE GUANAJUATO

León, Guanajuato a 24 de julio de 2020

Dr. David Delepine
División de Ciencias e Ingenierías
Director

Por medio de la presente le informo que considero que el documento de tesis que presenta **Jonathan Ulises Álvarez Martínez**, con título *Design, fabrication and implementation of microfluidics systems applied in chemical micromixers and particle sorters test*, reúne los requisitos para proceder a su defensa en examen para obtener el grado de Maestro en Ciencias Aplicadas, por lo que como sinodal doy mi aval para continuar con este proceso.

Agradeciendo su atención quedo a sus órdenes para cualquier aclaración

Atentamente,
"La Verdad Os Hará Libres"

Dr. Francisco Alarcón Oseguera
Profesor Titular A
SNI Nivel I
Departamento de Ingeniería Física

División de Ciencias e Ingenierías, Campus León
Loma del Bosque 103, Col. Lomas del Campestre, León, Gto, México, C.P. 37150
Tel. 01 (477) 788-5100 Ext. 8476 Fax. Ext. 8410
www.ugto.mx

Campus León | División de Ciencias e Ingenierías
Departamento de Ingeniería Física

León, Gto., México a 28 de julio de 2020

Archivo: GGJ 30/20
Asunto: Revisión de Tesis

Dr. David Yves Ghislain Delepine
Director
División de Ciencias e Ingenierías
Universidad de Guanajuato-Campus León
Estimado Dr. Delepine

Después de haber leído la tesis titulada **"Design, fabrication and implementation of microfluidic systems applied in chemical micromixers and particle sorters"**, que para obtener el grado de Maestro en Ciencias Aplicadas escribió el Licenciado en Ingeniería Física Jonathan Ulises Álvarez Martínez, de la manera más atenta, me permito comentar qué en esta tesis se reporta el diseño, desarrollo y caracterización de un dispositivo microfluídico capaz de transportar dos fluidos, que dependiendo de las condiciones a las que se encuentran se pueden mezclar por el proceso de difusión o mantenerse separados. Para lograr este desarrollo tecnológico, Jonathan y su asesor tuvieron que diseñar e implementar equipo adicional el cual se encuentra localizado en laboratorio de Biofotoacústica. Además, en la entrevista que tuve con Jonathan para que me aclarará dudas sobre el tema que investigó, me percate que domina el tema de manera sobresaliente, mostrando conocimiento, habilidades, actitudes y valores muy superiores a las de otros estudiantes a los que les he revisado su tesis. Por último, le comento que todas las correcciones que le pidi hiciera ya están incluidas en el texto de la tesis.

Por lo anterior, esta tesis reúne todas las características de una tesis de la Maestría en Ciencias Aplicadas y la apruebo para su presentación ante el comité designado para este fin.

ATENTAMENTE
"LA VERDAD OS HARÁ LIBRES"
EL PROFESOR

Dr. Gerardo Gutiérrez Juárez
Profesor Titular B

c. c. p. Archivo GGJ

Loma del Bosque 103
Lomas del Campestre, León, Gto.
Ap. Postal E-143, C.P. 37000
Tel. (477) 788-5100 ext. 8513 & 8488
Fax. (477) 788-5100 ext. 8410
http://www.fisica.ugto.mx/~ggutj

Bibliography

Au, Anthony K et al. (2016). "3D-printed microfluidics". In: *Angewandte Chemie International Edition* 55.12, pp. 3862–3881.

Bahei Islami, Sima and Salman Ahmadi (2019). "The effect of flow parameters on mixing degree of a three dimensional rhombus micromixer with obstacles in the middle of the mixing channel using oscillatory inlet velocities". In: *Transp Phenom Nano Micro Scales* 7.1, pp. 62–71.

Baroud, Charles N et al. (2003). "Reaction-diffusion dynamics: Confrontation between theory and experiment in a microfluidic reactor". In: *Physical Review E* 67.6, p. 060104.

Bhattacharjee, Nirveek et al. (2016). "The upcoming 3D-printing revolution in microfluidics". In: *Lab on a Chip* 16.10, pp. 1720–1742.

Bruus, Henrik (2008). *Theoretical microfluidics*. Vol. 18. Oxford university press Oxford.

Camarena-Chávez, Victor A et al. (2020). "Implementation and assessment of a low-cost 3D laser platform controlled by open software for printing polymeric microstructures". In: *Journal of Micromechanics and Microengineering* 30.3, p. 035010.

Capretto, Lorenzo et al. (2011). "Micromixing within microfluidic devices". In: *Microfluidics*. Springer, pp. 27–68.

Chabinyc, Michael L et al. (2001). "An integrated fluorescence detection system in poly (dimethylsiloxane) for microfluidic applications". In: *Analytical chemistry* 73.18, pp. 4491–4498.

Dauyeshova, Bagdagul, Luis R Rojas-Solórzano, and Ernesto Monaco (2018). "Numerical simulation of diffusion process in T-shaped micromixer using Shan-Chen Lattice Boltzmann Method". In: *Computers & Fluids* 167, pp. 229–240.

Di Leonardo, R et al. (2006). "Multipoint holographic optical velocimetry in microfluidic systems". In: *Physical review letters* 96.13, p. 134502.

Do, Mai Trang (2015). "Fabrication of submicrometer 3D structures by one-photon absorption direct laser writing and applications". PhD thesis. Laboratoire de Photonique Quantique et Moleculaire (UMR 8537 CNRS) ECOLE NORMALE SUP ERIEURE DE CACHAN.

Fang, Wei-Feng et al. (2011). "Characterization of microfluidic mixing and reaction in microchannels via analysis of cross-sectional patterns". In: *Biomicrofluidics* 5.1, p. 014111.

Foreman, Matthew R et al. (2008). "Inversion of the Debye-Wolf diffraction integral using an eigenfunction representation of the electric fields in the focal region". In: *Optics express* 16.7, pp. 4901–4917.

Fourkas, John T (2020). "Fundamentals of two-photon fabrication". In: *Three-Dimensional Microfabrication Using Two-photon Polymerization*. Elsevier, pp. 57–76.

Gendron, P-O, F Avaltroni, and KJ Wilkinson (2008). "Diffusion coefficients of several rhodamine derivatives as determined by pulsed field gradient–nuclear magnetic resonance and fluorescence correlation spectroscopy". In: *Journal of fluorescence* 18.6, p. 1093.

Gong, Hua et al. (2017). "Custom 3D printer and resin for 18 μm$\times$ 20 μm microfluidic flow channels". In: *Lab on a Chip* 17.17, pp. 2899–2909.

Groisman, Alex and Stephen R Quake (2004). "A microfluidic rectifier: anisotropic flow resistance at low Reynolds numbers". In: *Physical review letters* 92.9, p. 094501.

Hessel, Volker, Holger Löwe, and Friedhelm Schönfeld (2005). "Micromixers—a review on passive and active mixing principles". In: *Chemical Engineering Science* 60.8-9, pp. 2479–2501.

Holmes, Andrew S (2001). "Laser fabrication and assembly processes for MEMS". In: *Laser Applications in Microelectronic and Optoelectronic Manufacturing VI*. Vol. 4274. International Society for Optics and Photonics, pp. 297–306.

Hong, Bo et al. (2016). "A concentration gradient generator on a paper-based microfluidic chip coupled with cell culture microarray for high-throughput drug screening". In: *Biomedical microdevices* 18.1, p. 21.

Hossain, Shakhawat et al. (2020). "Investigation of mixing performance of two-dimensional micromixer using Tesla structures with different shapes of obstacles". In: *Industrial & Engineering Chemistry Research*.

Hübner, Jörg et al. (2001). "Integrated optical measurement system for fluorescence spectroscopy in microfluidic channels". In: *Review of Scientific Instruments* 72.1, pp. 229–233.

Inguva, Venkatesh et al. (2018). "Computer design of microfluidic mixers for protein/RNA folding studies". In: *PloS one* 13.6.

Isiksacan, Ziya et al. (2016). "Rapid fabrication of microfluidic PDMS devices from reusable PDMS molds using laser ablation". In: *Journal of Micromechanics and Microengineering* 26.3, p. 035008.

Joanni, Ednan et al. (2015). "Fabrication of molds for PDMS microfluidic devices by laser swelling of PMMA". In: *Rsc Advances* 5.32, pp. 25089–25096.

Keller, Stephan et al. (2008). "Processing of thin SU-8 films". In: *Journal of micromechanics and microengineering* 18.12, p. 125020.

Keshmiri, Kiarash et al. (2019). "Microfluidics to determine the diffusive mass transfer of a low viscosity solvent into a high viscosity hydrocarbon". In: *Fuel* 235, pp. 1327–1336.

Kim, Eunhee et al. (2016). "Nano-patterned SU-8 surface using nanosphere-lithography for enhanced neuronal cell growth". In: *Nanotechnology* 27.17, p. 175303.

Kim, Pilnam et al. (2008). "Soft lithography for microfluidics: a review". In:

Kirby, Daniel et al. (2012). "Centrifugo-magnetophoretic particle separation". In: *Microfluidics and nanofluidics* 13.6, pp. 899–908.

Kishimoto, Satoshi et al. (2009). "Fabrication of micromodel grid for various moiré methods by femtosecond laser exposure". In: *Optics letters* 34.1, pp. 112–114.

Kumaran, V and P Bandaru (2016). "Ultra-fast microfluidic mixing by soft-wall turbulence". In: *Chemical Engineering Science* 149, pp. 156–168.

Kuntaegowdanahalli, Sathyakumar S et al. (2009). "Inertial microfluidics for continuous particle separation in spiral microchannels". In: *Lab on a Chip* 9.20, pp. 2973–2980.

LaFratta, Christopher N and Tommaso Baldacchini (2017). "Two-photon polymerization metrology: Characterization methods of mechanisms and microstructures". In: *Micromachines* 8.4, p. 101.

LaFratta, Christopher N et al. (2015). "A convenient direct laser writing system for the creation of microfluidic masters". In: *Microfluidics and Nanofluidics* 19.2, pp. 419–426.

Lagus, Todd P and Jon F Edd (2013). "A review of the theory, methods and recent applications of high-throughput single-cell droplet microfluidics". In: *Journal of Physics D: Applied Physics* 46.11, p. 114005.

Lee, Chia-Yen et al. (2011). "Microfluidic mixing: a review". In: *International journal of molecular sciences* 12.5, pp. 3263–3287.

Lee, Chia-Yen et al. (2016). "Passive mixers in microfluidic systems: A review". In: *Chemical Engineering Journal* 288, pp. 146–160.

Lee, Jaesung, Sarah E Mena, and Mark A Burns (2019). "Micro-particle operations Using Asymmetric traps". In: *Scientific reports* 9.

Lee, Kwang-Sup et al. (2006). "Recent developments in the use of two-photon polymerization in precise 2D and 3D microfabrications". In: *Polymers for advanced technologies* 17.2, pp. 72–82.

Lei, Lei et al. (2020). "Experimental and simulation study of flow patterns in the combined flow focusing and T-junction device". In: *Journal of Micromechanics and Microengineering* 30.5, p. 055001.

Li, Qinggele (2014). "Optimization of point spread function of a high numerical aperture objective lens:" PhD thesis. Laboratoire de Photonique Quantique et Moleculaire (UMR 8537 CNRS) ECOLE NORMALE SUP ERIEURE DE CACHAN.

Li, Yong-Jiang et al. (2013). "Transport of dynamic biochemical signals in steady flow in a shallow Y-shaped microfluidic channel: effect of transverse diffusion and longitudinal dispersion". In: *Journal of biomechanical engineering* 135.12.

Liaros, Nikolaos and John T Fourkas (2019). "Ten years of two-color photolithography". In: *Optical Materials Express* 9.7, pp. 3006–3020.

Lim, Miles P et al. (2018). "Augmenting mask-based lithography with direct laser writing to increase resolution and speed". In: *Optics express* 26.6, pp. 7085–7090.

Lin, Yibo et al. (2017). "Stitch aware detailed placement for multiple e-beam lithography". In: *Integration* 58, pp. 47–54.

MacDonald, Michael P, Gabriel C Spalding, and Kishan Dholakia (2003). "Microfluidic sorting in an optical lattice". In: *Nature* 426.6965, pp. 421–424.

Mao, Fei et al. (2017). "LOPA-based direct laser writing of multi-dimensional and multi-functional photonic submicrostructures". In: *Advanced Fabrication Technologies for Micro/Nano Optics and Photonics X*. Vol. 10115. International Society for Optics and Photonics, p. 1011509.

Mata, Alvaro, Aaron J Fleischman, and Shuvo Roy (2005). "Characterization of polydimethylsiloxane (PDMS) properties for biomedical micro/nanosystems". In: *Biomedical microdevices* 7.4, pp. 281–293.

MICROCHEM (2017). *Datasheet*. urlhttp://web.mit.edu/3.042/team$1_0$8f/*documents*/$SU8-2050.pdf$.

Nguyen, Dam Thuy Trang et al. (2016). "One-step fabrication of submicrostructures by low one-photon absorption direct laser writing technique with local thermal effect". In: *Journal of Applied Physics* 119.1, p. 013101.

Nguyen, Nam-Trung, Xiaoyang Huang, and Toh Kok Chuan (2002). "MEMS-micropumps: a review". In: *J. Fluids Eng.* 124.2, pp. 384–392.

Nguyen, Nam-Trung and Zhigang Wu (2004). "Micromixers—a review". In: *Journal of micromechanics and microengineering* 15.2, R1.

Noonan, David P et al. (2011). "A modular, mechatronic joint design for a flexible access platform for MIS". In: *2011 IEEE/RSJ International Conference on Intelligent Robots and Systems*. IEEE, pp. 949–954.

Papautsky, Ian, Tim Ameel, and A Bruno Frazier (2001). "A review of laminar single-phase flow in microchannels". In: *ASME, Proceedings of Int. Mech. Eng Congress Expos Proc (IMECE)*. Vol. 2, pp. 3067–3075.

Parida, Om Prakash and Navakant Bhat (2009). "Characterization of optical properties of SU-8 and fabrication of optical components". In: *Int. Conf. on Opt. and Photon.(CSIO)*, pp. 4–7.

Parittotokkaporn, Sam et al. (2019). "Make it simple: long-term stable gradient generation in a microfluidic microdevice". In: *Biomedical microdevices* 21.3, p. 77.

Prakash, Shaurya, Marie Pinti, and Bharat Bhushan (2012). "Theory, fabrication and applications of microfluidic and nanofluidic biosensors". In: *Philosophical Transactions of the Royal Society A: Mathematical, Physical and Engineering Sciences* 370.1967, pp. 2269–2303.

Sánchez, M Florencia and Dolores C Carrer (2016). "Lipid Bilayer Patterns Fabrication by One-Photon Lithography". In: *Chemical and Synthetic Approaches in Membrane Biology*. Springer, pp. 37–48.

Shi, Jinjie et al. (2009). "Continuous particle separation in a microfluidic channel via standing surface acoustic waves (SSAW)". In: *Lab on a Chip* 9.23, pp. 3354–3359.

Shi, Xianchun et al. (2019). "A novel passive micromixer with array of Koch fractal obstacles in microchannel". In: *Journal of Dispersion Science and Technology*, pp. 1–12.

Shields IV, C Wyatt, Catherine D Reyes, and Gabriel P López (2015). "Microfluidic cell sorting: a review of the advances in the separation of cells from debulking to rare cell isolation". In: *Lab on a Chip* 15.5, pp. 1230–1249.

Somaweera, Himali, Akif Ibraguimov, and Dimitri Pappas (2016). "A review of chemical gradient systems for cell analysis". In: *Analytica chimica acta* 907, pp. 7–17.

Strachan, BRIONY C et al. (2019). "Improved expansion of T cells in culture when isolated with an equipment-free, high-throughput, flow-through microfluidic module versus traditional density gradient centrifugation". In: *Cytotherapy* 21.2, pp. 234–245.

Suryawanshi, Prashant L et al. (2018). "A review on microreactors: Reactor fabrication, design, and cutting-edge applications". In: *Chemical Engineering Science* 189, pp. 431–448.

Tong, Quang Cong et al. (2017). "Rapid direct laser writing of desired plasmonic nanostructures". In: *Optics letters* 42.12, pp. 2382–2385.

Trivedi, Mahendra Kumar et al. (2015). "The potential impact of biofield treatment on human brain tumor cells: A time-lapse video microscopy". In:

Wang, David W and John C Tsai (2004). *Optical grating fabrication*. US Patent 6,748,138.

Wang, GR, Fang Yang, and Wei Zhao (2014). "There can be turbulence in microfluidics at low Reynolds number". In: *Lab on a Chip* 14.8, pp. 1452–1458.

Wangikar, Sandeep Sitaram, Promod Kumar Patowari, and Rahul Dev Misra (2018). "Numerical and experimental investigations on the performance of a serpentine microchannel with semicircular obstacles". In: *Microsystem Technologies* 24.8, pp. 3307–3320.

Wolf, Emil and Yajun Li (1981). "Conditions for the validity of the Debye integral representation of focused fields". In: *Optics Communications* 39.4, pp. 205–210.

Wu, Jing et al. (2016). "Biochemical analysis on microfluidic chips". In: *TrAC Trends in Analytical Chemistry* 80, pp. 213–231.

Yee, Daryl W et al. (2017). "Functionalized 3D Architected Materials via Thiol-Michael Addition and Two-Photon Lithography". In: *Advanced Materials* 29.16, p. 1605293.

Zaidon, Nuradawiyah et al. (2016). "Serpentine microfluidic structures for concentration gradient generators". In: *2016 Symposium on Design, Test, Integration and Packaging of MEMS/MOEMS (DTIP)*. IEEE, pp. 1–5.

Zhang, Jun et al. (2016). "Fundamentals and applications of inertial microfluidics: a review". In: *Lab on a Chip* 16.1, pp. 10–34.

Zhang, Xunli et al. (2006). "Continuous flow separation of particles within an asymmetric microfluidic device". In: *Lab on a Chip* 6.4, pp. 561–566.

Zimmerman, William BJ (2006). *Microfluidics: history, theory and applications*. Vol. 466. Springer Science & Business Media.